



HHS Public Access

Author manuscript

FASEB J. Author manuscript; available in PMC 2025 April 30.

Published in final edited form as:

FASEB J. 2024 April 30; 38(8): e23606. doi:10.1096/fj.202302260RR.

Rhodopsin Mislocalization Drives Ciliary Dysregulation in a Novel Autosomal Dominant Retinitis Pigmentosa Knock-In Mouse Model

Shimpei Takita^{1,3}, Sultana Jahan¹, Sanae Imanishi^{1,3}, Hemavathy Harikrishnan^{1,3}, David LePage⁵, Rachel J. Mann⁵, Ronald A. Conlon⁵, Masaru Miyagi⁴, Yoshikazu Imanishi^{1,2,3,**}

¹Department of Ophthalmology, Eugene and Marilyn Glick Eye Institute, Indiana University School of Medicine, Indianapolis, IN 46202, USA;

²Department of Pharmacology and Toxicology, Indiana University School of Medicine, Indianapolis, IN 46202, USA;

³Stark Neurosciences Research Institute, Indiana University School of Medicine, Indianapolis, IN 46202, USA;

⁴Department of Pharmacology, Case Western Reserve University, Cleveland, Ohio 44106, USA;

⁵Department of Genetics and Genome Sciences, Case Western Reserve University, Cleveland, Ohio 44106, USA

Abstract

Rhodopsin mislocalization encompasses various blind conditions. Rhodopsin mislocalization is the primary factor leading to rod photoreceptor dysfunction and degeneration in autosomal dominant retinitis pigmentosa (adRP) caused by class I mutations. In this study, we report a new knock-in mouse model that harbors a class I Q344X mutation in the endogenous rhodopsin gene, which causes rod photoreceptor degeneration in an autosomal dominant pattern. In *Rho*^{Q344X/+} mice, mRNA transcripts from the wild-type (*Rho*) and *Rho*^{Q344X} mutant rhodopsin alleles are expressed at equal levels. However, the amount of RHO^{Q344X} mutant protein is 2.7 times lower than that of wild-type rhodopsin, a finding consistent with the rapid degradation of the mutant protein. Immunofluorescence microscopy indicates that RHO^{Q344X} is mislocalized to the inner segment and outer nuclear layers of rod photoreceptors both in *Rho*^{Q344X/+} and *Rho*^{Q344X/Q344X} mice, confirming the essential role of the C-terminal VxPx motif in promoting OS delivery of rhodopsin. The mislocalization of RHO^{Q344X} is associated with the concurrent mislocalization of wild-type rhodopsin in *Rho*^{Q344X/+} mice. To understand the global changes in proteostasis,

**Corresponding author: Yoshikazu Imanishi (yimanish@iu.edu).

Author Contributions

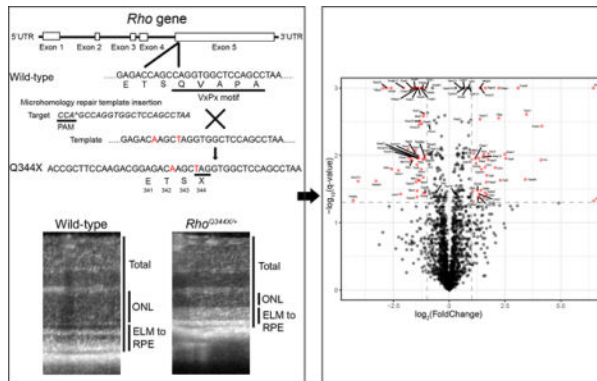
ST performed mRNA, OCT, histology, immunoblots, and proteomics experiments, and analyzed the data. SJ, RC, DL, RJM, and YI generated the *Rho*^{Q344X} knock-in mouse strain. SJ and YI established the *Rho*^{Q344X} knock-in mouse strain. SJ studied and analyzed the genome of the mouse strain. SI conducted rhodopsin-related immunohistochemical experiments and analyzed the data. HH assisted in analyzing data relevant to PCR, OCT, histology and immunoblots. MM aided in experimental design and data interpretation for the proteomics. YI conceptualized and designed the study. YI aided in the data interpretation throughout the manuscript. The manuscript was written by ST, SJ, SI, MM, and YI.

DISCLOSURES

The authors declare no conflicts of interests.

we conducted quantitative proteomics analysis and found attenuated expression of rod-specific OS membrane proteins accompanying reduced expression of ciliopathy causative gene products, including constituents of BBSome and axonemal dynein subunit. Those studies unveil a novel negative feedback regulation involving ciliopathy-associated proteins. In this process, a defect in the trafficking signal leads to a reduced quantity of the trafficking apparatus, culminating in a widespread reduction in the transport of ciliary proteins.

Graphical Abstract



A novel knock-in mouse model has been generated expressing a rhodopsin mutant prone to mislocalization. This model has enabled us to analyze alterations in the retinal proteome that affect the transport of rhodopsin and other proteins toward the photoreceptor sensory cilia.

Introduction

The mislocalization of rhodopsin has been identified in both human subjects and animal models suffering from a range of vision-impairing conditions. These include inherited retinal degeneration, retinal damage caused by light exposure, and retinal detachment (1–8). In retinitis pigmentosa (RP), rhodopsin mislocalization is observed in various forms of genetic conditions, including but not limited to those with mutations in the rhodopsin gene (*Rho*) (6). Rhodopsin mislocalization is the cause of photoreceptor dysfunction and degeneration, as demonstrated by various animal models manifesting defects in rhodopsin transport. For example, rhodopsin mislocalization is especially prominent in animal models with rhodopsin mutations collectively categorized as class I (9–11), which alter or delete the C-terminal (Ct) tail region of rhodopsin (12–14). Class I mutations, such as Q344X mutation (*Rho*^{Q344X}), disrupt the trafficking signal VxPx required to effectively transport rhodopsin to the rod outer segments (OSs) (14–16). Because of the trafficking deficiency, rhodopsin in these mice localizes aberrantly to the plasma membrane and other endomembrane structures of rod inner segments (16).

The majority of these animals are transgenic animals generated through pronuclear injections, which result in copy number variations and transgene incorporation into random chromosomal locations that may negatively or positively affect the expression levels (10). As overexpression of wild-type rhodopsin protein can cause photoreceptor degeneration (17), careful assessment of rhodopsin quantities, both from wild-type and mutant gene,

are necessary for the study of rod degeneration in transgenic animals (11). Phenotypic outcomes of class I mutant rhodopsin transgenics are also variable, with one showing no rhodopsin mislocalization to non-OS compartments (10), and others recapitulating rhodopsin mislocalization (9, 11). A mouse model with human rhodopsin knock-in allele (*hRho*^{Q344X}) harboring a class I mutation Q344X was also established and characterized previously (18, 19). While expression of mutated rhodopsin is regulated under the endogenous rhodopsin promoter, 5' non-coding region of the *hRho*^{Q344X} mRNA had an interruption by the LoxP sequence, which attenuated the translation of the mutated rhodopsin allele by one order of magnitude (18, 20). Consistent with the low expression of the mutant allele, the heterozygote *hRho*^{Q344X/+} knock-in mouse demonstrated only minimal degeneration (18) consistent with a loss of rhodopsin function (21, 22), and did not appear to show a toxic gain of function as expected for autosomal dominant RP (adRP) model (23). Those findings strengthen the notion that precise regulation of both mutated and wild-type alleles is essential for understanding the degrees of rod dysfunction and degeneration in rhodopsin-mediated adRP.

To establish a model for adRP triggered by a toxic gain-of-function class I mutation, we took advantage of CRISPR (clustered regularly interspaced short palindromic repeats)-Cas9 system and have created a novel knock-in mouse carrying the *Rho*^{Q344X} mutation in its endogenous rhodopsin gene. In the retinas of these heterozygous *Rho*^{Q344X/+} knock-in mice, both wild-type and mutant alleles are expressed in roughly equal amounts, mirroring what is expected in human patients with point mutations in non-promoter regions of the rhodopsin gene. Our findings indicate that this new mouse model accurately recapitulates the progressive degeneration of rod photoreceptors typically seen in rhodopsin adRP patients and the *Rho*^{P23H} adRP mouse model (23). Moreover, homozygous mutant mice exhibit accelerated loss of rod photoreceptor cells, thereby confirming the dose-dependent toxicity of the *Rho*^{Q344X} mutation. Using a high-throughput proteomic approach, we identified proteomics changes caused by the *Rho*^{Q344X} mutation, providing insights into the molecular pathways attenuated or activated in the retina. Consequently, this new *Rho*^{Q344X} knock-in mouse model is a valuable tool for studying rod photoreceptor degeneration and rhodopsin transport defects that occur in adRP patients.

Materials and methods

Animals

All animal experiments conducted adhered to the procedures approved by the Institutional Animal Care and Use Committee (IACUC) at Case Western Reserve University or Indiana University School of Medicine and were in compliance with the guidelines set forth by both the American Veterinary Medical Association Panel on Euthanasia and the Association for Research in Vision and Ophthalmology. The mice were housed under a 12-hour light/12-hour dark (7 a.m./7 p.m.) cycle and received standard mouse chow. We confirmed that the mice used in this study do not carry rd1 and rd8 mutations (24, 25).

Generation of *Rho*^{Q344X/+} knock-in mice

Class I mutations are located near the Ct region of rhodopsin. To select guides that direct Cas9 nuclease to cut near the desired insertion point, the genomic sequence surrounding the translation stop codon of the rhodopsin gene was analyzed using the CRISPOR algorithm (<http://crispor.tefor.net/>). Four candidate guides were designed and screened: 103/rev, 5'-GTCTCTGGCCAGGCTTAGGC-3'; 98/fw, 5'-CAAGACGGAGACCAGCCAGG-3'; 93/rev, 5'-AGGCTTAGGCTGGAGCCACC-3'; 89/rev, 5'-TTAGGCTGGAGCCACCTGGC-3'. The cutting efficiencies of candidate guides were evaluated using the Guide-it sgRNA screening system (Clontech). Upon screening, 89/rev guide was selected, and a large-scale sgRNA suitable for injection into mouse zygotes was prepared by PNA Bio. A single-stranded 100 bp microhomology DNA template (ACTGGGAGATGACGACGCCTCTGCCACCGCTTCCAAGACGGAGACAAAGCTAGGTGGCTCCAGCCTAAGCCTGGCCAGAGACTGTGGCTGAAAGTAGGAGT, mutations introduced to the original genomic sequence are underlined.) was synthesized and PAGE purified (Integrated DNA Technologies (IDT)). Following the validation of the large-scale sgRNA preparation, mixes of Cas9 protein (PNA Bio, CP01–20), sgRNA, and oligonucleotide template was injected into one-cell stage C57BL/6J mouse embryos in the Case Transgenic and Targeting Facility. Following standard transgenic practice, the concentrations of the constituents of the mixtures were varied from 20–5 ng/μL Cas9 protein, 20–5 ng/μL sgRNA, and 20–5 ng/μL oligonucleotide. Following injections, embryos were recovered and surgically transferred into the oviducts of pseudo-pregnant recipient females (CD1). The resulting pups were weaned at P21 and were screened for precise integration by genomic PCR as described below. F1 progeny from founder animals were then subjected to DNA sequencing to verify the absence of sequence alterations surrounding the integration site. Three independent F1 lines were then established, maintained under C57BL/6J background, and used for further studies. To reduce the potential off-target effects of CRISPR-Cas9-mediated gene editing, the mice underwent a minimum of three backcrosses with the wild-type C57BL/6 strain.

Screening and genotyping of *Rho*^{Q344X} knock-in mice

For the screening of a founder animal and genotyping of mice carrying *Rho*^{Q344X} allele, genomic DNA was extracted from the tails of mice following the procedure described previously (26). Genomic DNA was subjected to PCR (forward primer, Q344X geno-F (5'-GCATCCACAGGACACATGGA-3'); reverse primer, Q344X geno-R (5'-TGTCATGTTCCCTGATAGACAAGCT-3')) to amplify 598 bp fragment, covering 289 bp upstream and 309 bp downstream of the CRISPR-Cas9 cleavage site. Wild-type allele has a BsaI restriction site (GAGACC); the cleavage of which results in 318 and 280 bp fragments. The *Rho*^{Q344X} allele (GAGACA) lacks a BsaI restriction site, rendering this allele resistant to BsaI.

Examination of wild-type and Q344X mutant *Rho* mRNA expression levels in the *Rho*^{Q344X/+} retinas

We amplified the region encompassing the stop codons by RT-PCR. Total retinal RNA was extracted from *Rho*^{Q344X/+} mice at P35 and reverse transcribed into

cDNA using SuperScript IV reverse transcriptase (ThermoFisher Scientific). A fragment of 438 bp common to both wild-type and Q344X mutant *Rho* mRNA was PCR-amplified for 16 cycles by using a primer pair designed in exons 4 and 5 (forward primer, 5'- GCTTCCCTACGCCAGTGTG-3'; reverse primer, 5'- GGGGAGCCTCATTGCTTTCA-3'). The resulting products underwent digestion with the BsaI restriction enzyme or remained untreated overnight at 37 °C, and were then used as templates for quantitative PCR (qPCR). BsaI restriction enzyme cuts only wild-type fragment while Q344X fragment remains uncut with BsaI digestion. Consequently, the samples digested with BsaI contain only the unmodified Q344X mutant fragments, while the untreated samples retain both the wild-type and the Q344X fragments intact. To accurately determine the ratio of Q344X to wild-type fragments, both digested and undigested DNA samples were subjected to qPCR using the above primer pair. This qPCR assay employed a CYBR Green-based protocol (27) using QuantStudio™ 6 Flex Real-Time PCR System (ThermoFisher Scientific) following the manufacture's protocol, facilitating the quantitative comparison of these specific DNA fragments. The ratio of Q344X and wild-type cDNAs was derived from these results.

Optical Coherence Tomography (OCT)

Wild-type, *Rho*^{Q344X/+}, and *Rho*^{Q344X/Q344X} mice were anesthetized with isoflurane, and their pupils were dilated using 0.5% tropicamide and 2.5% phenylephrine. OCT images of these mice were captured at different postnatal days (P21, P35, P60, P90, P120, and P360) using the Phoenix Research Labs Reveal Optical Coherence Tomography (OCT2) Imaging System (Micron IV, Phoenix Research Laboratories, Pleasanton, CA, USA). To evaluate entire and ONL retinal thicknesses, cross-sectional retinal images passing through the optic nerve head (ONH) were obtained in dorsal-ventral and nasal-temporal axes. OCT images were captured using the line type and full line size settings with an average of 60 frames/scan. Enhanced Depth Imaging was selected to improve the signal originating from the outer retina. The acquired OCT images were segmented for retinal layers and analyzed using InSight software (Voxeleron LLC). Points 500 µm from the ONH (nasal, temporal, ventral, and dorsal) were used for the comparison.

Morphometry by light microscopy

Wild-type and *Rho*^{Q344X/+} mice were sacrificed at P35 and P90, and their eyes were removed. Eyecups were prepared and fixed in 4% paraformaldehyde/PB for 6 hrs, washed by PBS 3 times, and embedded in 1.5% agarose. Eyecup sections with a thickness of 40 µm were prepared using a vibratome (7000 SMZ, Campden Instruments, UK). Sections were cut in the dorsal-ventral axis, and those passing through the ONH were used for further analysis. The samples were stained with Hoechst 33342 (50 ng/mL in PBS), and mounted on glass bottom dish with VECTASHIELD® PLUS Antifade Mounting Medium (Vector Laboratories). Images were acquired with AX R confocal microscope (Nikon) using 20x Apo Lambda S (NA = 0.95) water immersion objective lens. The thicknesses of the ONL were measured in four sections prepared from four independent mice for each genotype and time point. Thicknesses of the ONL were measured at 150 µm intervals using NIS-Elements (Nikon).

Mass spectrometric analysis of retinal proteins

For the proteomic analysis of the retina, four mice ($n = 4$) were employed per genotype, specifically for the wild-type and *Rho*^{Q344X/+} genotypes. Retinas were collected from P35 mice in PBS, were snap-frozen in liquid nitrogen and stored at -80°C until use. Retinal proteins were extracted from the retinas using 50 μL of RIPA buffer. For each sample, the supernatant was collected after centrifugation ($20,000 \times g$, 4°C , 10 min). The remaining proteins in the pellet was further extracted with 50 μL of 8M urea, 50 mM Tris-HCl (pH 8.5). Following another round of centrifugation ($20,000 \times g$, 4°C , 10 min), the resultant supernatant was collected and combined with the supernatant obtained from the initial extraction with RIPA buffer. Protein concentrations were measured by Protein Assay Dye Reagent (Bio-Rad, #5000006) and 50 μg samples were subjected to SDS-PAGE until the protein bands had migrated approximately 1 cm into 10% Mini-PROTEAN Precast Gels (Bio-Rad, #4561033). The top 1 cm of the gel was then excised for each lane and in-gel digested by trypsin (28). Following digestion, peptides were extracted from the gels and subjected to LC-MS/MS using the ThermoScientific Fusion Lumos mass spectrometry system in the Proteomics Core facility of the Cleveland Clinic Foundation as described previously (29).

Proteins were identified by comparing all of the experimental peptide MS/MS spectra against the NCBI mouse protein database using the Andromeda search engine integrated into the MaxQuant version 2.2.0.0. Carbamidomethylation of cysteine was set as a fixed modification, whereas variable modifications included oxidation of methionine to methionine sulfoxide and acetylation of N-terminal amino groups. For protein identification, strict trypsin specificity was applied. The minimum peptide length was set to 7, the maximum missed cleavage was set to 2, the cutoff false discovery rate was set to 0.01, and match between runs (match time window: 0.7 min; alignment time window: 20 min) was enabled. The label-free quantitation (LFQ) option was enabled to adjust the integrated peptide intensities by the total ion current (TIC) of each sample, correcting for variations in sample loading and injection (30). The LFQ minimum ratio count was set to 2. The remaining parameters were kept as default.

Protein quantitation was accomplished using Perseus (version 2.0.7.0) (31). LFQ values were \log_2 -transformed. Proteins with at least three data points out of four in either of the groups (wild-type or *Rho*^{Q344X/+}) were selected. Subsequently, missing values were imputed using the “Replace missing value from normal distribution” function on the entire matrix with default parameters. The resulting data were then subjected to two-sample t-test. Using the output from Perseus, pathway analyses were performed in R (version 3.3.0+) using the clusterProfiler package (32), via the RStudio interface (version 4.3.1).

Immunoblot analysis

Proteins were extracted from the retinas as described in the section above (four mice per genotype). The retinal extracts, consisting of 20 μg proteins, were resolved by SDS-PAGE (130V, 1.5 hr) and transferred to PVDF membranes (0.4 A, 75 min). After blocking with 5% skim milk in TBS containing 0.1% (v/v) Tween-20 (0.1% TBST, pH 7.4) for 1 hr at room temperature, the membranes were incubated with B6-30 or 1D4 antibody for

overnight at 4 °C. Then the membrane was incubated with HRP-labeled goat anti-mouse or anti-rabbit secondary antibodies (1:5000 dilution) for 1 hr. Target proteins were detected with ChemiDoc (Bio-Rad). After detecting target proteins, the membrane was stripped with stripping buffer (ThermoFisher Scientific, 46430), blocked, reacted, and detected with anti- β -tubulin antibody, E7, for internal control.

Immunofluorescence microscopy

Mouse eyecups were fixed with 4% formaldehyde solution containing 5% sucrose in PBS (136 mM NaCl, 2.68 mM KCl, 8.1 mM Na₂HPO₄, 8 mM Na₂HOP₄, and 1.4 mM KH₂PO₄) for 5–6 hrs at 4 °C. Subsequently, the samples were incubated in a series of PBS buffers with gradually increasing sucrose concentrations, ranging from 5% to 20%, at 4°C. After incubation with 20 % sucrose in PBS, eyecups were infiltrated with a 1:2 mixture of Tissue-Tek O.C.T. compound (Sakura Finetek) and 20 % sucrose in PBS, and then frozen in liquid nitrogen-chilled isopentane. Frozen eyecups were stored at –80 °C until their usage. Cryosections (12 – 16 μ m thickness) were prepared with a Leica CM3050S cryostat (Leica). Then, sections were stored at –80 °C until usage. Cryosections were thawed and air dried at 37 °C for 40 min. For immunohistochemistry, sections were first blocked with PBS containing 5 % goat serum, 0.3 % Triton X, and 0.02 % sodium azide for 20 minutes, then incubated with primary antibodies diluted in PBST (PBS containing 0.1 % TritonX and 0.02 % sodium azide) for 1 – 3 days at 4 °C. Following antibodies were employed in this study: 1D4 (3 μ g/mL, anti-Ct rhodopsin) B6–30 (3 μ g/mL, anti-N-terminal rhodopsin, a kind gift from Dr. David Salom at the University of California Irvine); anti-NKA α 1 mouse a5 (Hybridoma Bank) or M7 (Santa Cruz) monoclonal antibody (1:500 dilution); anti-ROM1 rabbit polyclonal antibody (1:500 dilution; Abcam, ab220049); anti-GFAP rabbit polyclonal antibody (1:500 dilution; DAKO, Z0334); anti-BBS7 rabbit polyclonal antibody (1:500 dilution; Proteintech, 18961–1-AP); anti-BBS9 rabbit polyclonal antibody (1:500 dilution; Atlas Antibodies, HPA021289); anti-Gt1 α (GNAT1) mouse monoclonal antibody (1:1000 dilution; Santa Cruz, sc-136143); anti-RP1 (RP1 axonemal microtubule associated) chicken polyclonal antibody (1:2000 dilution; a kind gift from Dr. Eric A. Pierce at Harvard Medical School); anti-PDE6 γ rabbit polyclonal antibody (1:1000 dilution; ABR Affinity BioReagents). Sections were rinsed with PBST once and washed with the same solution for 5 minutes four times. Then, they were incubated with 18 μ g/mL of Hoechst 33342 and secondary antibodies diluted in PBST overnight at 4 °C. Following secondary antibodies were used: 3 μ g/mL of Cy3 conjugated goat anti-mouse IgG; Alexa Fluor 488 donkey anti-mouse antibody (1:1500 dilution; ThermoFisher); Alexa Fluor 488 donkey anti-rabbit antibody (1:1500 dilution; Jackson ImmunoResearch); Cy3 donkey anti-mouse antibody (1:1500 dilution; Jackson ImmunoResearch); Cy3 donkey anti-rabbit antibody (1:1500 dilution; Jackson ImmunoResearch); Cy3 goat anti-chicken antibody (1:1500 dilution; Jackson ImmunoResearch). Sections were rinsed with PBST once and washed with the same solution for 5 minutes four times, mounted with VECTASHIELD® PLUS Antifade Mounting Medium (Vector Laboratories), and then covered with # 1.5 cover glass. The samples were imaged with Nikon AX R confocal microscopy system (Nikon) using 40X Apo LWD Lambda S (NA = 1.15) water lens with pinhole size 17.9 μ m at 0.3 μ m/pixel with 0.3 μ m Z step. For NKA and GFAP staining, images were also acquired with LSM 700 (Zeiss) laser scanning confocal microscope system using EC Plan-Neofluar 40x oil

lens (NA = 1.30). The images were max projections of z-stacks. Brightness and contrast were adjusted using the Image J Fiji. The identical settings were applied to images within the same panels. For quantitative analyses of immunofluorescence signals originating from anti-NKA, GNAT1, BBS7, and BBS9 antibodies, signal intensities from the IS, INL/GCL region (NKA), the entire photoreceptor (GNAT1), or the entire retina (BBS7 and BBS9) were measured and integrated for P35 wild-type and *Rho*^{Q344X/+} mice (four mice per genotype) using ImageJ (33). Retinal regions spanning 227 μm on the horizontal axis were selected for measurements. Background signals were measured from a region in the same image where the specimen was not present and were subtracted from each measurement.

The lengths of RP1-positive axonemes in P21 wild-type and *Rho*^{Q344X/+} mice were measured manually using polyline function in the Annotations and Measurements tool of the NIS-Elements software (Nikon). Ten axonemes of photoreceptors were measured in each animal, resulting in a total of 40 cilia (n = 40 from 4 animals per genotype) being used for the comparison between wild-type and *Rho*^{Q344X/+} mice.

Statistical Analysis

Statistical analyses and data visualization were conducted using GraphPad Prism software (version 8.0). One-way ANOVA with Tukey's post hoc test was used for multi-group comparisons, and an unpaired two-tailed t-test for two-group comparisons, unless specified in the figure legends. The *p*-values of less than 0.05 were considered significant. The data were reported as the mean \pm SD.

Results

Generation of a knock-in mouse model for Q344X mutation in the endogenous rhodopsin gene

We edited the mouse rhodopsin gene (*Rho*) allele, resulting in a class I rhodopsin mutation Q344X (*Rho*^{Q344X}) (12) (Figure 1). This mutation introduced a premature stop codon that truncates the last five amino acids, including the Ct VxPx cilia targeting signal (34, 35). The CRISPR-Cas9 system was used to mutate the *Rho* gene, repairing the induced DNA break through microhomology-mediated end joining by a template containing desired mutations (Figure 1A, red). The DNA microhomology template was designed to introduce a point mutation, causing a replacement of Glutamine (Q) at the amino acid position 344 with a stop codon (X) (Figure 1B). To prevent cleavage of the *Rho*^{Q344X} gene by CRISPR-Cas9, the template was designed to introduce an additional silent C to A mutation at the third nucleotide of the codon for threonine 342. This silent mutation eliminated the BsaI restriction site as verified using PCR fragments amplified from the genomic DNA of *Rho*^{Q344/+} mice (Figure 1C, lane 1 and 2). For wild-type (*Rho*^{+/+}) mice, the PCR products were completely digested (Figure 1C, lanes 3 and 4). Sequence analysis of the allele confirmed the successful introduction of the Q344X mutation to the endogenous rhodopsin gene (Figure 1B). Moreover, we verified the successful transcription of the *Rho*^{Q344X} mRNA by sequencing the cDNA derived from the retina. We also amplified the region containing the Q344X mutation site using retinal cDNA prepared from *Rho*^{Q344X/+} mice at P35. In *Rho*^{Q344X/+} mice, the ratio between BsaI-resistant and digested fragments

was approximately 1:1 (Figure 1D, left). Using quantitative PCR assay, the relative amounts of wild-type and Q344X mRNA expressed in *Rho*^{Q344X/+} mice were $48.6 \pm 3.6\%$ and $51.4 \pm 8.6\%$, respectively, with no statistically significant difference (Figure 1D, right; $p = 0.6164$, $n = 3$ mice). Those results indicate that the *Rho*^{Q344X} allele is expressed at a level similar to the wild-type *Rho* allele, as expected for an adRP model. We also subcloned PCR fragments derived from the region around position 344, and randomly selected and sequenced 51 clones. Among them, 29 were derived from the *Rho*^{Q344X} allele, whereas 21 were from the wild-type *Rho* allele, further validating that both alleles are expressed at similar levels.

Degeneration of rod photoreceptors in *Rho*^{Q344X/+} knock-in mice

The loss of rod photoreceptor cells is the major cause of vision impairment in RP. To assess the rate and extent of rod degeneration, *Rho*^{Q344X/+} and *Rho*^{Q344X/Q344X} mice were imaged by OCT at different postnatal days (P21 – P360) and compared with age-matching wild-type (*Rho*^{+/+}) mice. In the retinas of *Rho*^{Q344X/+} mice, outer nuclear layer (ONL) thickness gradually decreased over time (Figure 2A and B). The retina degeneration was assessed in four different regions located in the nasal, temporal, ventral, and dorsal regions of the retina (Figure 2C, 1 – 4). From P21 onwards, there was a noticeable decrease in the thickness of the ONL in *Rho*^{Q344X/+} mice (Figure 2D, magenta). The thickness of ONL decreased by 18.7–27.0% at P35 and became progressively thinner (Figure 2D), with a nearly 45.6–57.4 % decrease at P90 (Figure 2D). We also compared the degree of rod degeneration in the dorsoventral axis of the retina. Unlike rhodopsin class II mutant (*Rho*^{P23H/+}) knock-in mice, which exhibit severe rod degeneration in the ventral region from P35 onwards (23, 36), *Rho*^{Q344X/+} mice showed similar degrees of rod degeneration (Supplemental Figure S1) in dorsal and ventral regions from P35 – P60 ($p > 0.2$). Subsequent observations revealed higher degree of rod degeneration in the dorsal region than in the ventral region at P90 ($p < 0.001$) and P120 ($p < 0.0001$). By P360, however, the dorsoventral difference became insignificant ($p > 0.5$), with over 91% of photoreceptors lost in both the dorsal and ventral regions.

The *Rho*^{Q344X/Q344X} mutant mice showed even more rapid degeneration than *Rho*^{Q344X/+} (Figure 2A and D). At P21, the ONL thicknesses of *Rho*^{Q344X/Q344X} mice were 3.8–5.0 times thinner than those of wild-type mice (Figure 2D, compare green and blue) in the four regions (Figure 2C), suggesting that rod degeneration began earlier than P21 with the ONL layer almost entirely lost by P35. Given that 97% of the nuclei in the ONL are associated with rod cells (37), these results indicate rods degenerated in *Rho*^{Q344X/+} and *Rho*^{Q344X/Q344X} mice.

To measure the extent of cell loss, we also compared the ONL thicknesses between wild-type and *Rho*^{Q344X/+} mice in different dorsoventral regions at P35 and P90 using confocal microscopy (Figure 3), which provides better contrasts and resolution for discriminating retinal layers. Consistent with the result we obtained by OCT, *Rho*^{Q344X/+} mice lost around 35% of nuclei in their ONL at P35 and 48.7% at P90 (Figures 3A and B). Consistent with the observations made by OCT (Figure 2), the dorsal regions—located at 0.75, 1.05, 1.35, and 1.50 mm from the ONH—exhibited more severe photoreceptor loss compared to

the corresponding ventral regions at P90 (Figure 3B, $p < 0.05$, as determined by two-way ANOVA with post hoc Šidák test).

The VxPx motif (VAPA in murine rhodopsin), which is missing in Q344X rhodopsin, is required for the effective transport of rhodopsin to the OSs (9, 11, 15, 16, 34). To study the effect of this truncation to the protein transport, we studied the localization of rhodopsin in the *Rho*^{Q344X/+} retina by immunofluorescence confocal microscopy. To understand the distribution of wild-type rhodopsin, we employed the 1D4 monoclonal antibody against wild-type, *Rho*^{Q344X/+} and *Rho*^{Q344X/Q344X} mice at P24, when there are still surviving rod photoreceptor cells in *Rho*^{Q344X/Q344X} mice. As expected, wild-type rhodopsin was localized specifically to the OSs of wild-type mice (Figure 4A, left panels). In *Rho*^{Q344X/Q344X} mice, specific signals were not detected in the photoreceptor layer. This observation is consistent with the truncation of the Ct tail in RHO^{Q344X}, which abolished the epitope of the 1D4 antibody. In *Rho*^{Q344X/+} mice, wild-type rhodopsin was primarily localized to the OS, however, a trace amount of wild-type rhodopsin was also observed in the IS, ONL and OPL. We introduced the B6–30 antibody that was raised against the Nt region of wild-type rhodopsin, which is retained in RHO^{Q344X}. We observed OS-specific signals in wild-type mice, which only express wild-type rhodopsin. B6–30 labeled OS, IS, ONL and OPL of *Rho*^{Q344X/Q344X} mice, which only expresses RHO^{Q344X} mutant protein (Figure 4B, left panels). Within *Rho*^{Q344X/+} mice, the B6–30 antibody showed more pronounced IS, ONL and OPL mislocalization than the 1D4 antibody did. On P62 – 63, we observed a similar mislocalization trend in *Rho*^{Q344X/+} mice (Figure 4A and B, right panels). The B6–30 antibody demonstrated more pronounced mislocalization than the 1D4 antibody did. Those results of *Rho*^{Q344X/+} and *Rho*^{Q344X/Q344X} mice indicate RHO^{Q344X} is prone to mislocalize into rod photoreceptors, verifying the role of the VxPx motif in OS-directed transport of rhodopsin. In *Rho*^{Q344X/+} mice, RHO^{Q344X} causes the mislocalization of wild-type RHO, although the extent of this mislocalization is less pronounced than that of RHO^{Q344X} itself.

Rhodopsin is the most abundant constituent of the OS, which is transported together with lipids (38), and decrease in transport of rhodopsin results in the shortening or loss of OS structures (21, 22). In *Rho*^{Q344/+} mice, we found that the OS layer was approximately 50% thinner than in wild-type mice at P35 (Figure 3D). We also investigated the OS structures of *Rho*^{Q344X/Q344X} mice at P21. At this stage of *Rho*^{Q344X/Q344X} mice, about 25% of rods are still surviving (Figure 2), nevertheless the thickness of the OS layer is less than 3% of that observed in P35 wild-type mice (Figure 3C and D). The presence of OSs was confirmed by immunofluorescence microscopy, employing an antibody against the OS marker PDE6 γ (Figure 3C right, red), which localized above the ONL where RHO^{Q344X} was detected by the B6–30 antibody (Figure 3C right, green). The extent of OS volume loss in *Rho*^{Q344X/+} and *Rho*^{Q344X/Q344X} mice is analogous to that in rhodopsin heterozygote and homozygote knockout mice (21, 22), respectively, consistent with significantly compromised rhodopsin transport due to the deficiency in the VxPx OS trafficking signal.

Instability of mutant Rhodopsin in *Rho*^{Q344X/+} mice

We have previously demonstrated that the mislocalization of rhodopsin disrupts its homeostasis, thereby triggering alternative lysosome-mediated pathways for degradation

(39). However, the extent to which this process influences the expression levels of wild-type and RHO^{Q344X} rhodopsin remains unclear. To address the issue, Rhodopsin expression was analyzed by immunoblots employing B6–30 and 1D4 monoclonal antibodies against rhodopsin to quantify the protein levels. Using the B6–30 antibody which recognizes both wild-type (RHO) and Q344X (RHO^{Q344X}) rhodopsin, we found that the level of total rhodopsin in *Rho*^{Q344X/+} is approximately 37.5% of that in wild-type mice (Figure 5A). We utilized 1D4 monoclonal antibody to determine to what degree wild-type rhodopsin is accountable for the total rhodopsin observed in *Rho*^{Q344X/+} retina. This antibody specifically targets the Ct region of rhodopsin, which is made up of residue 341–348 (40). As the 1D4 antibody recognizes the Ct part only preserved in wild-type rhodopsin, this observation suggests that the amount of wild-type rhodopsin present in *Rho*^{Q344X/+} mice was approximately 27.0% of that in wild-type mice (Figure 5B). Inferring from these data, the amount of RHO^{Q344X} mutant rhodopsin protein is approximately 2.7-fold lower than that of wild-type rhodopsin protein in *Rho*^{Q344X/+} mice ($p = 0.022$) (Figure 5C). Considering the similar expression levels of mRNA transcripts from *Rho*^{Q344X} and wild-type alleles (Figure 1D), these results suggest a decreased stability of the Q344X mutant protein compared to its wild-type counterpart in individual rod cells. As control, we studied the amount of rhodopsin in the retinas of *Rho*^{P23H/+} knock-in mice (23) using B6–30 and 1D4 antibodies. Those two antibodies generated similar amounts of signals in *Rho*^{P23H/+} retinas (Figure 5A and B, green bars, B6–30 RHO^{P23H/+} vs 1D4 RHO^{P23H/+}, $p = 0.159$ by unpaired t-test), because they can recognize RHO^{P23H} protein equally.

To compare the relative amounts of proteins in *Rho*^{Q344X/+} and wild-type mice more unbiasedly, we subjected retinal protein extracts at P35 to proteomic analysis. Based on this quantitative proteomics study, rhodopsin quantity decreased by 66.7 % (Table 1), confirming the general instability of rhodopsin in the *Rho*^{Q344X/+} retina (Figure 5). By immunofluorescence microscopy conducted at P24 and P62 – 63, however, we noted that the total signal from RHO, detected by the B6–30 antibody, is similar between *Rho*^{Q344X/+} and wild-type mice (Figure 4). In the tightly packed disc membranes of outer segments, the labeling of rhodopsin by antibodies is inefficient. This issue is visibly apparent in *Xenopus laevis*, where the larger rod outer segments make the problem more noticeable, although other species experience similar challenges (41). The inadequate labeling could be due to the antibodies' limited ability to penetrate these densely packed disc membranes (41). Additionally, epitope masking, potentially caused by a clouding effect or protein aggregation (42), may also play a role in this inefficiency, especially considering that rhodopsin concentrations can reach as high as 4 mM (43). These factors collectively pose significant challenges to accurately quantifying rhodopsin using immunofluorescence, particularly in outer segments. Therefore, we opted not to conduct immunofluorescence quantification of rhodopsin.

We previously reported downregulation of sodium potassium ATPase (NKA) in *Xenopus* rod photoreceptors expressing human Rho^{Q344X} protein due to co-degradation of NKA with mislocalized rhodopsin. Immunofluorescence microscopy employing NKA alpha antibody demonstrates immunofluorescence originating from ISs was approximately 31.4 % weaker in *Rho*^{Q344X/+} than in wild-type (Figures 6A– C, $p < 0.05$). In *Rho*^{Q344X/+} mice, when measured in whole retinas by mass spectrometry, sodium potassium ATPase alpha subunits

1 – 3 showed no significant difference in their expression levels between *Rho*^{Q344X/+} and wild-type mice. This lack of difference is potentially due to compensatory changes in non-photoreceptor regions of the retina, as *Rho*^{Q344X/+} mice showed a trend of increased NKA in ganglion cell and inner nuclear layers (Figure 6C), albeit the difference was not statistically significant ($p > 0.2$).

The effects of rhodopsin mistrafficking on OS defects and retinal degeneration was further confirmed through immunofluorescence microscopy. We observed reduction of retinal outer segment membrane protein 1 (ROM1), an OS marker, in *Rho*^{Q344X/+} mice, indicating rod OS shortening. However, unlike rhodopsin, ROM1 did not mislocalize to the IS and ONL (Figures 6A and B). Consistent with the rod photoreceptor degeneration, an upregulation of glial fibrillary acidic protein (GFAP) was confirmed. GFAP is a common indicator of reactive gliosis in response to retinal pathogenesis (Figure 6D and E, compare wild-type and *Rho*^{Q344X/+}).

***Rho*^{Q344X/+} mutation has impact on proteins involved in the structure and function of photoreceptor sensory cilia**

To study the biological changes in *Rho*^{Q344X/+} mice in an unbiased manner, we conducted quantitative mass spectrometry analyses of retinal proteins at P35, when retinas are experiencing ongoing degeneration. A total of 1917 proteins were identified and quantified both in wild-type and *Rho*^{Q344X/+} knock-in retinas by MaxQuant (Figure 7A and Supplemental Table S2). Among them, 89 proteins were differentially expressed between wild-type and *Rho*^{Q344X/+} retinas significantly (q -value < 0.05 and $2 >$ fold change). Through pathway analysis employing GO terms (Supplemental Figure S2), proteins involved in visual perception and light stimulus detection (e.g., GO0007601 and GO0009583), visual system development (e.g., GO0150063), and photoreceptor cell maintenance (e.g., GO0045494) exhibited significant alterations (Figures 7B and C). These findings are consistent with rod photoreceptors being the primary cells impacted by the Q344X mutant rhodopsin protein. Regarding GO terms relevant to cellular components, proteins associated with ciliary structures are most frequently observed (e.g., GO0097733), being consistent with *Rho*^{Q344X} causing ciliary malfunction. Regarding molecular functions, proteins were enriched in terms relevant to phototransduction or visual cycle, such as PDE activity, retinoid binding, and isoprenoid binding. While the majority of these pathways are relevant to the core of photoreceptor structure and functions, proteins involved in glial cell differentiation (GO0010001) were enriched (Figure 7C). Based on specific analyses of individual gene products (Table 1), rod photoreceptor outer segment proteins showed high degrees of losses that cannot be explained solely by the degeneration of photoreceptors (Figures 2 and 3). Those proteins include phosphodiesterase 6 alpha (PDE6 α , 42.4% wild-type) and beta subunits (PDE6 β , 42.7% wild-type), rod cGMP-gated channel alpha (CNGA1, 33.3% wild-type) and beta subunit (CNGB, 41.9% wild-type), rhodopsin kinase (GRK1, 48.0% wild-type), rod transducin alpha (GNAT1, 34.4% wild-type), beta (GNB1, 44.8% wild-type), and gamma subunits (GNGT1, 31.1% wild-type), Guanylate cyclase 1 (RetGC1, also known as Gucy2e, 39.2% wild-type) and Guanylate cyclase 2 (RetGC2, also known as Gucy2f, 40.2% wild-type), regulator of G protein signaling 9 (RGS9, 34.8% wild-type), and ATP-binding cassette transporter 4 (ABCA4, 37.5% wild-type). Regarding GNAT1, we

verified the result using immunofluorescence microscopy, which demonstrated a similar degree of downregulation (Supplemental Figure S3). Those observations are consistent with thinning of the outer segment layer, which occurs largely as a result of rhodopsin downregulation. Consistent with OS shortening, OS structural proteins Peripherin (PRPH2) and ROM1 demonstrated dramatic downregulation by 27.8–37.0%. Consistent with low trafficking activities of *Rho*^{Q344X/+} photoreceptors, proteins involved in ciliary transport of transmembrane proteins were downregulated; those proteins included Bardet-Biedl syndrome (BBS) 1 BBS1 (36.8% wild-type), BBS7 (45.2% wild-type), and BBS9 (39.3% wild-type), that are constituents of BBSome (44). The proteomic results for BBS7 and BBS9 were further validated through immunofluorescence microscopy employing the antibodies that successfully labeled these proteins in the mouse retina (45). This analysis revealed that BBS7 and BBS9 have similar localization patterns in the wild-type photoreceptors, and that expressions of these proteins were significantly downregulated in the rod ISs and OSs, as well as throughout the entire retinas of *Rho*^{Q344X/+} mice (Supplemental Figures S3A–C). Moreover, Dynein axonemal heavy chain 5 (DNAH5), a ciliary motor component, was significantly downregulated (42.3% wild-type). In line with this reduction in axonemal dynein, our analysis demonstrated that ciliary axonemes, identified as RP1 protein-positive structures through immunofluorescence microscopy (46), were markedly shorter in *Rho*^{Q344X/+} mice ($5.11 \pm 0.71 \mu\text{m}$) relative to their wild-type counterparts ($7.08 \pm 0.77 \mu\text{m}$) as early as P21 (Supplemental Figures S3 D and E).

We discovered that proteins localized to the inner segment of photoreceptors exhibit less pronounced alterations compared to those in the photoreceptor sensory cilia. Specifically, retinol dehydrogenase 12 (RDH12), an inner segment protein in photoreceptors (55.1% wild-type), and inosine monophosphate dehydrogenase 1 (IMPDH1, 59.3% wild-type), which is primarily localized to non-outer segment compartments of photoreceptors, which is mostly localized to non-OS compartments of photoreceptors under normal light conditions (47). Rod arrestin (Arrestin 1, also known as Sag), a soluble protein in photoreceptors, showed about 33.7% decrease (66.3% wild-type) which is consistent with the degree of rod photoreceptor cell loss around this stage. Those results indicate that *Rho*^{Q344X/+} is demonstrating OS-directed trafficking defects, both of integral membrane and membrane-associated proteins. Minimal changes were observed for GNAT2, which is a cone-specific transducin alpha subunit (Table 1). This observation is consistent with the specific expression of *Rho*^{Q344X} in rod photoreceptors, which is the primary cell type affected in *Rho*^{Q344X/+} mice.

While the downregulated proteins expressed in rods are indicative of dysfunction and dysregulation in rod photoreceptor neurons, we identified several proteins that were significantly upregulated in *Rho*^{Q344X/+} mice (Table 1). Among the most prominently elevated proteins are Pyruvate kinase M (PKM, 8816.5% wild-type), GFAP (466.5% wild-type), fibroblast growth factor 2 (FGF2, 488.0% wild-type), Clusterin (CLU, 1730.7% wild-type), alpha-N-acetylgalactosaminidase (NAGA, 468.6% wild-type), and Peroxiredoxin 4 (PRDX4, 1775.3% wild-type). Upregulation of one of these genes, GFAP, was consistent with the upregulation of the signal by immunofluorescence microscopy (Figures 6D and E, compare wild-type and *Rho*^{Q344X/+}). These genes are likely to play roles in neuroprotection, metabolic reprogramming, the mitigation of oxidative stress, and Müller cell-mediated

reactive gliosis (Figures 7B and C). These alterations align with protective mechanisms activated in response to rod photoreceptor degeneration.

Discussion

This study reports a new mouse model of adRP caused by a class I rhodopsin mutation. In this knock-in mouse, the 344th amino acid of the endogenous rhodopsin is modified to a stop codon, eliminating the VxPx OS transport signal (15, 34). Therefore, the mutant gene is expressed under the regulation of the endogenous rhodopsin promoter, resulting in rod degeneration in an autosomal dominant pattern as observed in human patients. In heterozygous *Rho*^{Q344X/+} mice, both wild-type and the Q344X mutant rhodopsin alleles exhibit similar levels of mRNA expression. This equivalence in expression enables us to adequately explore the role of RHO^{Q344X} in rod degeneration and dysfunction, providing a relevant mouse model for rhodopsin adRP. Localization analyses in *Rho*^{Q344X/+} and *Rho*^{Q344X/Q344X} mice reveal that RHO^{Q344X} has a propensity for mislocalization to non-OS compartments. Additionally, the *Rho*^{Q344X} mutation triggers mislocalization of wild-type rhodopsin (RHO), although to a lesser extent than RHO^{Q344X} itself. This wild-type rhodopsin mislocalization was not detected in the *Xenopus laevis* models heterologously expressing Q344X mutant of *Xenopus* (41) or human (16) *Rho*. This apparent difference among models is potentially due to different properties of mammalian and amphibian rhodopsin, and due to the dimerization of murine rhodopsin previously observed (48), as such interaction may result in co-transport of wild-type and RHO^{Q344X} mutant rhodopsin to non-OS compartments. Downregulation of the ciliary transport component, as observed in this study, may also contribute to compromised OS transport of wild-type rhodopsin. In *Rho*^{Q344X/+} mice, rod photoreceptor cells degenerate progressively as in the case of adRP. Approximately 18.7–27.0% of rods are lost at P35, and 38.2–50.9% at P60. The rate of degeneration is similar to that observed for *Rho*^{P23H/+} knock-in mouse, which represents class II rhodopsin mutations causing adRP (23). While *Rho*^{P23H/+} knock-in mouse exhibited more severe rod degeneration in the ventral region than in the dorsal region (23, 36), *Rho*^{Q344X/+} mouse demonstrated more pronounced degeneration in the dorsal region. As the ventral region receives more light than the dorsal region (49), this observation suggests that light is not the exacerbating factor of photoreceptor degeneration in *Rho*^{Q344X/+} mice under ambient conditions used for normal laboratory animal housing. Our findings align with clinical observations in human patients: Whereas the T4R, T17M, P23H and other rhodopsin mutations can induce light-dependent sector retinitis pigmentosa in dog, mouse, and human (49, 50), the Q344X and other class I mutations has not been reported to cause a comparable disorder in humans (51).

The current study indicates that expression levels of the *Rho*^{Q344X} gene play a critical role in the disease manifestation. By comparing *Rho*^{Q344X/+} and *Rho*^{Q344X/Q344X} mice, we demonstrated the gene dosage effect of the *Rho*^{Q344X} allele: *Rho*^{Q344X/Q344X} mice demonstrated much more rapid degeneration than *Rho*^{Q344X/+} mice, with over 76.8% of rod cells lost at P21, and the majority of rods lost by P35. Furthermore, the speed of rod degeneration is much faster than that by simple elimination of wild-type rhodopsin in rhodopsin homozygote knockout mouse models, which demonstrated only loss of less than 30% rod nuclei by P21 – 30 (21, 22, 52). Thus, the degeneration of rods in our model is due

to the toxicity of Rho^{Q344X} and not to the loss of wild-type rhodopsin function. Our studies are distinct from those conducted on other knock-in mice that harbor mutations in the Ct region of rhodopsin. For example, in the Q344X human rhodopsin mutant heterozygote knock-in mouse model, there is no significant loss of rod photoreceptors by postnatal week 10 (approximately P60) because of the low expression level of the Q344X human rhodopsin product, which is less than 10% of the endogenous rhodopsin (18). Similar results were obtained for a rhodopsin knock-in mouse model expressing the Ter349Glu readthrough mutant of human rhodopsin. In this model, the ciliary targeting motif VAPA is followed by an additional 51 amino acids (53). Heterozygote Ter349Glu knock-in mice demonstrated mild photoreceptor degeneration, in which about 10% of rods were lost by P84, in contrast to our model, in which P60 *Rho*^{Q344X/+} mice lost more than 38.2% of rods. This relatively mild degeneration phenotype of the past model is likely due to low expression of the mutant allele as discussed in the original literature (53). Moreover, Ter349Glu rhodopsin may be less toxic than Q344X rhodopsin because VxPx motif can still be partially functional even if additional amino acids follow it. We and others previously found that the ciliary targeting signal VxPx is functional for OS delivery of rhodopsin, even if it is followed by an additional sequence such as GFP or other fluorescent proteins (16, 54), and indeed a significant fraction of Ter349Glu rhodopsin is observed in the OS of *Xenopus* rods expressing this protein (53). Our model is also distinct from the previously generated class I mutant rhodopsin transgenic models, which harbor additional genes of class I mutant rhodopsin via pronuclear injection-mediated transgenesis (10, 11). By this approach, various lines expressing multiple copies of transgene were generated. For example, in one of the studies using Q344X rhodopsin transgenic mouse, the expression of the mutant allele is estimated to be 24% of the total rod opsin transcript (11). Our model was designed so that the upstream rhodopsin promoter and 5'-untranslated regions are untouched in the *Rho*^{Q344X} mutant gene. Still, the accurate gene expression measurements in individual rods are confounded by the loss of rods, which negatively impacts the overall expression of mutant RNA quantities in the retina. Therefore, by editing out a restriction site unique to wild-type allele, we were able to directly compare the ratio of wild-type and mutant transcripts, that is approximately 1:1. Taken together, our study outlines the importance of emulating the human genetic condition of adRP in which the endogenous rhodopsin gene is edited, and thus mutant and wild-type transcripts are expressed equally.

Despite similar mRNA expression levels of wild-type and *Rho*^{Q344X} mutant alleles, rhodopsin protein expression level is significantly lower in the *Rho*^{Q344X/+} mouse model than in wild-type mice. In *Rho*^{Q344X/+} mice at P35, the amount of rhodopsin protein in the photoreceptor cells is significantly lower than expected based on the extent of rod degeneration observed in the retina. We believe this disproportionate loss of the mutant protein is partly due to Q344X rhodopsin protein being more unstable than wild-type rhodopsin protein, resulting in 2 – 3-fold lower levels of mutant rhodopsin than wild-type protein in individual rods. Rhodopsin localized in the OSs is degraded by RPE cells. As mislocalized rhodopsin do not enter the OSs, those proteins are not degraded by the canonical phagocytosis mechanism. Based on our previous study of *Xenopus laevis* rods, mislocalized rhodopsin proteins have two paths for elimination from rods: degradation by intracellular lysosomes (39) and secretion to extracellular space as vesicles (10, 11, 55).

Q344X rhodopsin lacks the last five amino acids, of which VAPA sequence promotes OS targeting of rhodopsin (15, 16, 34). Thus, most Q344X rhodopsin molecules should be initially parked at non-OS membrane compartments in the rods. Nevertheless, unlike OSs which are the most membrane-rich organelle with several hundred of disk membranes, the rest of the rod cells do not have sufficient membrane volume to accommodate massively synthesized rhodopsin proteins. Therefore, in situations of disease, rods increase the activity of the intracellular degradation and secretory elimination system to compensate for the malfunction of OS transportation. In the past, assessing the comparative effects of the *Rho*^{Q344X} mutation on wild-type and RHO^{Q344X} mutant rhodopsin has been challenging, particularly within the *Xenopus laevis* model. The difficulty arises from the variable expression levels of mutant rhodopsin observed in individual transgenic *Xenopus laevis*, making a direct quantitative comparison between RHO^{Q344X} and endogenous wild-type rhodopsin problematic. Our study of mice clarifies that RHO^{Q344X} mutant rhodopsin is more unstable than wild-type rhodopsin when they co-exist, indicating these two proteins are largely eliminated by rods via different mechanisms.

Rhodopsin itself is critical for OS maintenance; animal models with reduced levels of it experience a loss or reduction of their outer segment volume (21, 22). In accordance with the significantly reduced amount of total rhodopsin protein, we found that essential phototransduction proteins are also dramatically downregulated in *Rho*^{Q344X/+} mice. The downregulation is partly explainable by trafficking defects of those proteins associated with rhodopsin transport. For example, RetGC1's interaction with rhodopsin is essential for its transport to OSs (56). Therefore, Compromised OS transport of *Rho*^{Q344X} rhodopsin molecules explains the decreased quantity of RetGC1 in OSs. We currently do not know if other membrane-associated or integral membrane proteins depend on rhodopsin for their OS transport; nevertheless, we found rod phosphodiesterase catalytic subunits, both alpha and beta, are down-regulated. Previous studies indicated that loss of photoreceptor-specific guanylate cyclases, RetGC1 and RetGC2, results in loss of rod phosphodiesterase from OSs (57). The loss of these membrane proteins is not due to the general downregulation of rod photoreceptor proteins. Arrestin-1, one of the abundant rod photoreceptor proteins, was decreased only at the degree expected from the loss of rods in *Rho*^{Q344X/+} mice. Arrestin-1, although it interacts with photoactivated rhodopsin, is a soluble protein. Perhaps it does not require disk membrane interaction for its stability. Overall, *Rho*^{Q344X/+} represents models of retinal ciliopathies, specifically addressing the defects in ciliary cargo transport. BBSome is a complex of proteins consisting of BBS1, BBS2, BBS4, BBS5, BBS7, BBS8, and BBS9 (44). We found that BBS1, BBS7, and BBS9, BBSome components, are simultaneously downregulated (44). BBS2, BBS4, and BBS17 deficient mice are deficient in BBSome and show decreased OS lengths and rhodopsin mislocalization (58–60). Moreover, axonemal dynein heavy chain, Dnah5, was significantly downregulated. Mutation of this gene is implicated in macular dystrophy and primary ciliary dyskinesia (61). Consistent with these cilia/axoneme defects, immunohistochemical analysis revealed the structural changes of axonemes associated with Rpl. Mutations in *Rpl* are the causes of retinopathies such as retinitis pigmentosa and macular dystrophy (62, 63). RP1-positive axonemes were shorter (~70% wild-type) in *Rho*^{Q344X/+} than in wild-type at the stage as early as P21. Thus, downregulation of ciliopathy causative gene products, which occurs concomitantly with

the trafficking signal defect of RHO^{Q344X}, would further attenuate the ciliary transport of rhodopsin and other OS constituents.

Based on our previous study of *Xenopus laevis* rods, sodium potassium ATPase is co-degraded with mislocalized rhodopsin, likely via the endolysosomal system. Intriguingly, quantitative proteomics did not indicate overt downregulation of NKA alpha subunits in the whole retina. Those are likely because NKA proteins expressed in other cell types are masking the changes that occurred in rod inner segments. Other inner segment dominant protein, RDH12, showed approximately 45% loss in *Rho*^{Q344X/+} mice, coinciding with the degree of photoreceptor loss. Such absence of coincidental loss is another evidence that NKA observed in the whole retina is largely contributed by non-photoreceptor cell types. Consistent with the studies of *Xenopus*, our immunofluorescence study indicated a reduction of NKA in the rod inner segment, further supporting the contribution of *Rho*^{Q344X/+} in facilitating the degradation of this protein.

While the downregulated proteins indicate a general reduction in OS protein transport and compromised rod functions, we also identified upregulated proteins that signify adaptive changes triggered by rod degeneration in *Rho*^{Q344X/+} mice. The elevation of GFAP, a hallmark of reactive gliosis, is a well-documented response in animal models of retinal injury (64). Both FGF2 and CLU, known for their neuroprotective effects on rod cells (65, 66), exhibit significant upregulation in the retinas of *Rho*^{Q344X/+} mice. The upregulation of the lysosomal enzyme NAGA may facilitate the deglycosylation and subsequent degradation of proteins containing *N*-acetylgalactosamine, though such modification has not been identified for bovine rhodopsin (67). While N-glycan of murine rhodopsin has not been characterized in detail, our observation is consistent with the findings that mislocalized rhodopsin facilitates lysosomal degradation of other glycoprotein(s), such as NKA, in rod cells (39). In healthy rod photoreceptor cells, which are characterized by the Warburg effect, glucose metabolism products support both anabolic processes and OS synthesis (68). PKM, which is significantly upregulated in *Rho*^{Q344X/+} mice, can aid in channeling pyruvate toward oxidative phosphorylation while synergistically acting with lactate dehydrogenase to potentially steer both glucose and pyruvate toward anabolic pathways (69). Aerobic glycolysis contributes to OS growth and maintenance by providing the essential building blocks for macromolecules. Alterations in retinal energy metabolism could serve as a compensatory mechanism to address the compromised OS structure observed in *Rho*^{Q344X/+} mice.

In summary, we have developed a new mouse model replicating the rhodopsin mislocalization observed in retinitis pigmentosa patients. Unlike the class II mutations, which generally cause protein misfolding (12, 13, 23, 36), class I mutant rhodopsin can properly fold and regenerate with 11-*cis*-retinal to form functional pigment (12, 13). However, it mislocalizes within rod cells (9). As rhodopsin mislocalization is a phenomenon observed across a wide range of patients with RP and retinal ciliopathies (6), this model is well-suited for evaluating potential treatments aimed at mitigating rod degeneration in RP (70). As previously reported for the *Xenopus laevis* model (39, 55), our research also confirms that murine rod cells possess a mechanism to reduce the levels of the mutated Q344X rhodopsin more effectively, surpassing the efficiency of the standard RPE-mediated

phagocytic process. It remains unclear whether this action serves as a protective measure against the disease or contributes to its onset. Previous studies suggest the latter (39). Further investigations will clarify the specific mechanisms underlying the disease as well as any inherent protective measures within rod photoreceptor cells.

Supplementary Material

Refer to Web version on PubMed Central for supplementary material.

Acknowledgment

We thank Ms. K. C. Lynn for her technical assistance in maintenance and genotyping of the mice used in this study. The E7 (deposited by Prof. M. Klymkowsky) and a5 (deposited by Prof. D.M Fambrough) monoclonal antibodies were obtained from the Developmental Studies Hybridoma Bank, created by the NICHD of the NIH and maintained at The University of Iowa, Department of Biology, Iowa City, IA 52242. We would like to thank Dr. David Salom at the University of California Irvine for sharing the B6-30 antibody. We would also like to thank Dr. Eric A. Pierce and Dr. Qin Liu (Massachusetts Eye and Ear, Harvard Medical School, Boston, MA, USA) for the anti-RP1 chicken antibody. Mass spectrometry data were acquired by the Proteomics and Metabolomics Core at the Lerner Research Institute of the Cleveland Clinic Foundation. We thank Drs. Belinda Willard and Ling Li for acquiring mass spectrometry data. The mass spectrometer was purchased via an NIH-shared instrument grant, S10 OD023436. This work was supported by grants from the National Eye Institute (R01EY029680 and R01EY028884 to YI). This work was partly supported by a Challenge Grant from Research to Prevent Blindness to the Department of Ophthalmology, Indiana University School of Medicine, and by an award from the Ralph W. and Grace M. Showalter Research Trust and the Indiana University School of Medicine to YI. This work was also partly supported by Cohen Pilot Grants in Macular Degeneration Research (to YI and SI) from the Department of Ophthalmology, Indiana University School of Medicine.

Data availability

The raw mass spectrometry proteomics data used in this study have been deposited to the ProteomeXchange Consortium via the MassIVE partner repository with the dataset identifier PXD046795. All identified proteins are listed in Supplemental Table S1.

A list of nonstandard abbreviations:

adRP	autosomal dominant retinitis pigmentosa
ELM	external limiting membrane
GCL	ganglion cell layer
INL	inner nuclear layer
IS	inner segment
LFQ	label-free quantitation
OCT	optical coherent tomography
ONH	optic nerve head
ONL	outer nuclear layer
OPL	outer plexiform layer
OS	outer segment

PAM	protospacer adjacent motif
RP	retinitis pigmentosa
RPE	retinal pigment epithelium

References:

1. Nir I, and Papermaster DS (1986) Immunocytochemical localization of opsin in the inner segment and ciliary plasma membrane of photoreceptors in retinas of rds mutant mice. *Invest Ophthalmol Vis Sci* 27, 836–840 [PubMed: 2939037]
2. Bowes C, van Veen T, and Farber DB (1988) Opsin, G-protein and 48-kDa protein in normal and rd mouse retinas: developmental expression of mRNAs and proteins and light/dark cycling of mRNAs. *Exp Eye Res* 47, 369–390 [PubMed: 2846333]
3. Nir I, Agarwal N, Sagie G, and Papermaster DS (1989) Opsin distribution and synthesis in degenerating photoreceptors of rd mutant mice. *Exp Eye Res* 49, 403–421 [PubMed: 2529133]
4. Lewis GP, Erickson PA, Anderson DH, and Fisher SK (1991) Opsin distribution and protein incorporation in photoreceptors after experimental retinal detachment. *Exp Eye Res* 53, 629–640 [PubMed: 1835933]
5. Edward DP, Lim K, Sawaguchi S, and Tso MO (1993) An immunohistochemical study of opsin in photoreceptor cells following light-induced retinal degeneration in the rat. *Graefes Arch Clin Exp Ophthalmol* 231, 289–294 [PubMed: 8319919]
6. Li ZY, Kljavin IJ, and Milam AH (1995) Rod photoreceptor neurite sprouting in retinitis pigmentosa. *J Neurosci* 15, 5429–5438 [PubMed: 7643192]
7. Fariss RN, Molday RS, Fisher SK, and Matsumoto B (1997) Evidence from normal and degenerating photoreceptors that two outer segment integral membrane proteins have separate transport pathways. *J Comp Neurol* 387, 148–156 [PubMed: 9331178]
8. Milam AH, Li ZY, and Fariss RN (1998) Histopathology of the human retina in retinitis pigmentosa. *Prog Retin Eye Res* 17, 175–205 [PubMed: 9695792]
9. Sung CH, Makino C, Baylor D, and Nathans J (1994) A rhodopsin gene mutation responsible for autosomal dominant retinitis pigmentosa results in a protein that is defective in localization to the photoreceptor outer segment. *J Neurosci* 14, 5818–5833 [PubMed: 7523628]
10. Li T, Snyder WK, Olsson JE, and Dryja TP (1996) Transgenic mice carrying the dominant rhodopsin mutation P347S: evidence for defective vectorial transport of rhodopsin to the outer segments. *Proc Natl Acad Sci U S A* 93, 14176–14181 [PubMed: 8943080]
11. Concepcion F, and Chen J (2010) Q344ter mutation causes mislocalization of rhodopsin molecules that are catalytically active: a mouse model of Q344ter-induced retinal degeneration. *PLoS One* 5, e10904 [PubMed: 20532191]
12. Sung CH, Davenport CM, Hennessey JC, Maumenee IH, Jacobson SG, Heckenlively JR, Nowakowski R, Fishman G, Gouras P, and Nathans J (1991) Rhodopsin mutations in autosomal dominant retinitis pigmentosa. *Proc Natl Acad Sci U S A* 88, 6481–6485 [PubMed: 1862076]
13. Sung CH, Davenport CM, and Nathans J (1993) Rhodopsin mutations responsible for autosomal dominant retinitis pigmentosa. Clustering of functional classes along the polypeptide chain. *J Biol Chem* 268, 26645–26649 [PubMed: 8253795]
14. Nemet I, Ropelewski P, and Imanishi Y (2015) Rhodopsin Trafficking and Mistrafficking: Signals, Molecular Components, and Mechanisms. *Prog Mol Biol Transl Sci* 132, 39–71 [PubMed: 26055054]
15. Tam BM, Moritz OL, Hurd LB, and Papermaster DS (2000) Identification of an outer segment targeting signal in the COOH terminus of rhodopsin using transgenic *Xenopus laevis*. *J Cell Biol* 151, 1369–1380 [PubMed: 11134067]
16. Lodowski KH, Lee R, Ropelewski P, Nemet I, Tian G, and Imanishi Y (2013) Signals governing the trafficking and mistrafficking of a ciliary GPCR, rhodopsin. *J Neurosci* 33, 13621–13638 [PubMed: 23966685]

17. Tan E, Wang Q, Quiambao AB, Xu X, Qtaishat NM, Peachey NS, Lem J, Fliesler SJ, Pepperberg DR, Naash MI, and Al-Ubaidi MR (2001) The relationship between opsin overexpression and photoreceptor degeneration. *Invest Ophthalmol Vis Sci* 42, 589–600 [PubMed: 11222515]
18. Sandoval IM, Price BA, Gross AK, Chan F, Sammons JD, Wilson JH, and Wensel TG (2014) Abrupt onset of mutations in a developmentally regulated gene during terminal differentiation of post-mitotic photoreceptor neurons in mice. *PLoS One* 9, e108135 [PubMed: 25264759]
19. Hollingsworth TJ, Hubbard MG, Levi HJ, White W, Wang X, Simpson R, Jablonski MM, and Gross AK (2021) Proinflammatory Pathways Are Activated in the Human Q344X Rhodopsin Knock-In Mouse Model of Retinitis Pigmentosa. *Biomolecules* 11
20. Chan F, Bradley A, Wensel TG, and Wilson JH (2004) Knock-in human rhodopsin-GFP fusions as mouse models for human disease and targets for gene therapy. *Proc Natl Acad Sci U S A* 101, 9109–9114 [PubMed: 15184660]
21. Humphries MM, Rancourt D, Farrar GJ, Kenna P, Hazel M, Bush RA, Sieving PA, Sheils DM, McNally N, Creighton P, Erven A, Boros A, Gulya K, Capecchi MR, and Humphries P (1997) Retinopathy induced in mice by targeted disruption of the rhodopsin gene. *Nat Genet* 15, 216–219 [PubMed: 9020854]
22. Lem J, Krasnoperova NV, Calvert PD, Kosaras B, Cameron DA, Nicolo M, Makino CL, and Sidman RL (1999) Morphological, physiological, and biochemical changes in rhodopsin knockout mice. *Proc Natl Acad Sci U S A* 96, 736–741 [PubMed: 9892703]
23. Sakami S, Maeda T, Bereta G, Okano K, Golczak M, Sumaroka A, Roman AJ, Cideciyan AV, Jacobson SG, and Palczewski K (2011) Probing mechanisms of photoreceptor degeneration in a new mouse model of the common form of autosomal dominant retinitis pigmentosa due to P23H opsin mutations. *J Biol Chem* 286, 10551–10567 [PubMed: 21224384]
24. Chang B, Hawes NL, Hurd RE, Davisson MT, Nusinowitz S, and Heckenlively JR (2002) Retinal degeneration mutants in the mouse. *Vision Res* 42, 517–525 [PubMed: 11853768]
25. Mattapallil MJ, Wawrousek EF, Chan CC, Zhao H, Roychoudhury J, Ferguson TA, and Caspi RR (2012) The Rd8 mutation of the *Crb1* gene is present in vendor lines of C57BL/6N mice and embryonic stem cells, and confounds ocular induced mutant phenotypes. *Invest Ophthalmol Vis Sci* 53, 2921–2927 [PubMed: 22447858]
26. Tian G, Lee R, Ropelewski P, and Imanishi Y (2016) Impairment of Vision in a Mouse Model of Usher Syndrome Type III. *Invest Ophthalmol Vis Sci* 57, 866–875 [PubMed: 26943149]
27. Takita S, and Seko Y (2020) *eyes (+/-) ; lrp5 (+/-)* Zebrafish Reveals *Lrp5* Can Be the Receptor of Retinol in the Visual Cycle. *Iscience* 23, 101762 [PubMed: 33251495]
28. Shevchenko A, Tomas H, Havlis J, Olsen JV, and Mann M (2006) In-gel digestion for mass spectrometric characterization of proteins and proteomes. *Nat Protoc* 1, 2856–2860 [PubMed: 17406544]
29. Lyu M, Su CC, Miyagi M, and Yu EW (2023) Simultaneous solving high-resolution structures of various enzymes from human kidney microsomes. *Life Sci Alliance* 6
30. Cox J, and Mann M (2008) MaxQuant enables high peptide identification rates, individualized p.p.b.-range mass accuracies and proteome-wide protein quantification. *Nat Biotechnol* 26, 1367–1372 [PubMed: 19029910]
31. Tyanova S, Temu T, Sinitcyn P, Carlson A, Hein MY, Geiger T, Mann M, and Cox J (2016) The Perseus computational platform for comprehensive analysis of (prote)omics data. *Nat Methods* 13, 731–740 [PubMed: 27348712]
32. Yu G, Wang LG, Han Y, and He QY (2012) clusterProfiler: an R package for comparing biological themes among gene clusters. *OMICS* 16, 284–287 [PubMed: 22455463]
33. Schindelin J, Arganda-Carreras I, Frise E, Kaynig V, Longair M, Pietzsch T, Preibisch S, Rueden C, Saalfeld S, Schmid B, Tinevez JY, White DJ, Hartenstein V, Eliceiri K, Tomancak P, and Cardona A (2012) Fiji: an open-source platform for biological-image analysis. *Nat Methods* 9, 676–682 [PubMed: 22743772]
34. Deretic D, Williams AH, Ransom N, Morel V, Hargrave PA, and Arendt A (2005) Rhodopsin C terminus, the site of mutations causing retinal disease, regulates trafficking by binding to ADP-ribosylation factor 4 (ARF4). *Proc Natl Acad Sci U S A* 102, 3301–3306 [PubMed: 15728366]

35. Mazelova J, Astuto-Gribble L, Inoue H, Tam BM, Schonteich E, Prekeris R, Moritz OL, Randazzo PA, and Deretic D (2009) Ciliary targeting motif VxPx directs assembly of a trafficking module through Arf4. *Embo J* 28, 183–192 [PubMed: 19153612]
36. Chiang WC, Kroeger H, Sakami S, Messah C, Yasumura D, Matthes MT, Coppinger JA, Palczewski K, LaVail MM, and Lin JH (2015) Robust Endoplasmic Reticulum-Associated Degradation of Rhodopsin Precedes Retinal Degeneration. *Mol Neurobiol* 52, 679–695 [PubMed: 25270370]
37. Carter-Dawson LD, and LaVail MM (1979) Rods and cones in the mouse retina. I. Structural analysis using light and electron microscopy. *J Comp Neurol* 188, 245–262 [PubMed: 500858]
38. Rodriguez de Turco EB, Deretic D, Bazan NG, and Papermaster DS (1997) Post-Golgi vesicles cotransport docosahexaenoyl-phospholipids and rhodopsin during frog photoreceptor membrane biogenesis. *J Biol Chem* 272, 10491–10497 [PubMed: 9099692]
39. Ropelewski P, and Imanishi Y (2019) Disrupted Plasma Membrane Protein Homeostasis in a *Xenopus Laevis* Model of Retinitis Pigmentosa. *J Neurosci* 39, 5581–5593 [PubMed: 31061086]
40. MacKenzie D, Arendt A, Hargrave P, McDowell JH, and Molday RS (1984) Localization of binding sites for carboxyl terminal specific anti-rhodopsin monoclonal antibodies using synthetic peptides. *Biochemistry* 23, 6544–6549 [PubMed: 6529569]
41. Tam BM, Xie G, Oprian DD, and Moritz OL (2006) Mislocalized rhodopsin does not require activation to cause retinal degeneration and neurite outgrowth in *Xenopus laevis*. *J Neurosci* 26, 203–209 [PubMed: 16399688]
42. Sarkar D, Kang J, Wassie AT, Schroeder ME, Peng Z, Tarr TB, Tang AH, Niederst ED, Young JZ, Su H, Park D, Yin P, Tsai LH, Blanpied TA, and Boyden ES (2022) Revealing nanostructures in brain tissue via protein decrowding by iterative expansion microscopy. *Nat Biomed Eng* 6, 1057–1073 [PubMed: 36038771]
43. Nickell S, Park PS, Baumeister W, and Palczewski K (2007) Three-dimensional architecture of murine rod outer segments determined by cryoelectron tomography. *J Cell Biol* 177, 917–925 [PubMed: 17535966]
44. Nachury MV, Loktev AV, Zhang Q, Westlake CJ, Peranen J, Merdes A, Slusarski DC, Scheller RH, Bazan JF, Sheffield VC, and Jackson PK (2007) A core complex of BBS proteins cooperates with the GTPase Rab8 to promote ciliary membrane biogenesis. *Cell* 129, 1201–1213 [PubMed: 17574030]
45. Hsu Y, Seo S, and Sheffield VC (2021) Photoreceptor cilia, in contrast to primary cilia, grant entry to a partially assembled BBSome. *Hum Mol Genet* 30, 87–102 [PubMed: 33517424]
46. Liu Q, Zhou J, Daiger SP, Farber DB, Heckenlively JR, Smith JE, Sullivan LS, Zuo J, Milam AH, and Pierce EA (2002) Identification and subcellular localization of the RP1 protein in human and mouse photoreceptors. *Invest Ophthalmol Vis Sci* 43, 22–32 [PubMed: 11773008]
47. Plana-Bonamaiso A, Lopez-Begines S, Fernandez-Justel D, Junza A, Soler-Tapia A, Andilla J, Loza-Alvarez P, Rosa JL, Miralles E, Casals I, Yanes O, de la Villa P, Buey RM, and Mendez A (2020) Post-translational regulation of retinal IMPDH1 in vivo to adjust GTP synthesis to illumination conditions. *Elife* 9
48. Fotiadis D, Liang Y, Filipek S, Saperstein DA, Engel A, and Palczewski K (2003) Atomic-force microscopy: Rhodopsin dimers in native disc membranes. *Nature* 421, 127–128 [PubMed: 12520290]
49. Orlans HO, and MacLaren RE (2020) Comment on: ‘Sector retinitis pigmentosa caused by mutations of the RHO gene’. *Eye (Lond)* 34, 1477–1478 [PubMed: 31659286]
50. Coussa RG, Basali D, Maeda A, DeBenedictis M, and Traboulsi EI (2019) Sector retinitis pigmentosa: Report of ten cases and a review of the literature. *Mol Vis* 25, 869–889 [PubMed: 31908405]
51. Berson EL, Rosner B, Sandberg MA, Weigel-DiFranco C, and Dryja TP (1991) Ocular findings in patients with autosomal dominant retinitis pigmentosa and rhodopsin, proline-347-leucine. *Am J Ophthalmol* 111, 614–623 [PubMed: 2021172]
52. Berger A, Cavallero S, Dominguez E, Barbe P, Simonutti M, Sahel JA, Sennlaub F, Raoul W, Paques M, and Bemelmans AP (2014) Spectral-domain optical coherence tomography of the

rodent eye: highlighting layers of the outer retina using signal averaging and comparison with histology. *PLoS One* 9, e96494 [PubMed: 24788712]

53. Hollingsworth TJ, and Gross AK (2013) The severe autosomal dominant retinitis pigmentosa rhodopsin mutant Ter349Glu mislocalizes and induces rapid rod cell death. *J Biol Chem* 288, 29047–29055 [PubMed: 23940033]
54. Jin S, McKee TD, and Oprian DD (2003) An improved rhodopsin/EGFP fusion protein for use in the generation of transgenic *Xenopus laevis*. *FEBS Lett* 542, 142–146 [PubMed: 12729914]
55. Ropelewski P, and Imanishi Y (2020) RPE Cells Engulf Microvesicles Secreted by Degenerating Rod Photoreceptors. *eNeuro* 7
56. Pearring JN, Spencer WJ, Lieu EC, and Arshavsky VY (2015) Guanylate cyclase 1 relies on rhodopsin for intracellular stability and ciliary trafficking. *Elife* 4
57. Baehr W, Karan S, Maeda T, Luo DG, Li S, Bronson JD, Watt CB, Yau KW, Frederick JM, and Palczewski K (2007) The function of guanylate cyclase 1 and guanylate cyclase 2 in rod and cone photoreceptors. *J Biol Chem* 282, 8837–8847 [PubMed: 17255100]
58. Mykityn K, Mullins RF, Andrews M, Chiang AP, Swiderski RE, Yang B, Braun T, Casavant T, Stone EM, and Sheffield VC (2004) Bardet-Biedl syndrome type 4 (BBS4)-null mice implicate Bbs4 in flagella formation but not global cilia assembly. *Proc Natl Acad Sci U S A* 101, 8664–8669 [PubMed: 15173597]
59. Nishimura DY, Fath M, Mullins RF, Searby C, Andrews M, Davis R, Andorf JL, Mykityn K, Swiderski RE, Yang B, Carmi R, Stone EM, and Sheffield VC (2004) Bbs2-null mice have neurosensory deficits, a defect in social dominance, and retinopathy associated with mislocalization of rhodopsin. *Proc Natl Acad Sci U S A* 101, 16588–16593 [PubMed: 15539463]
60. Datta P, Allamargot C, Hudson JS, Andersen EK, Bhattarai S, Drack AV, Sheffield VC, and Seo S (2015) Accumulation of non-outer segment proteins in the outer segment underlies photoreceptor degeneration in Bardet-Biedl syndrome. *Proc Natl Acad Sci U S A* 112, E4400–4409 [PubMed: 26216965]
61. Fan KC, Patel NA, Yannuzzi NA, Prakhunhungsit S, Negron CI, Basora E, Colin AA, Tekin M, and Berrocal AM (2019) A unique case of vision loss in a patient with hypotrichosis and juvenile macular dystrophy and primary ciliary dyskinesia. *Am J Ophthalmol Case Rep* 15, 100486 [PubMed: 31431935]
62. Liu Q, Zuo J, and Pierce EA (2004) The retinitis pigmentosa 1 protein is a photoreceptor microtubule-associated protein. *Journal of Neuroscience* 24, 6427–6436 [PubMed: 15269252]
63. Riera M, Abad-Morales V, Navarro R, Ruiz-Nogales S, Mendez-Vendrell P, Corcostegui B, and Pomares E (2020) Expanding the retinal phenotype of RP1: from retinitis pigmentosa to a novel and singular macular dystrophy. *Br J Ophthalmol* 104, 173–181 [PubMed: 31079053]
64. Verderber L, Johnson W, Mucke L, and Sarthy V (1995) Differential regulation of a glial fibrillary acidic protein-LacZ transgene in retinal astrocytes and Muller cells. *Invest Ophthalmol Vis Sci* 36, 1137–1143 [PubMed: 7730023]
65. Lau D, McGee LH, Zhou S, Rendahl KG, Manning WC, Escobedo JA, and Flannery JG (2000) Retinal degeneration is slowed in transgenic rats by AAV-mediated delivery of FGF-2. *Invest Ophthalmol Vis Sci* 41, 3622–3633 [PubMed: 11006261]
66. Vargas A, Kim HS, Baral E, Yu WQ, Craft CM, and Lee EJ (2017) Protective effect of clusterin on rod photoreceptor in rat model of retinitis pigmentosa. *PLoS One* 12, e0182389 [PubMed: 28767729]
67. Nakagawa M, Miyamoto T, Kusakabe R, Takasaki S, Takao T, Shichida Y, and Tsuda M (2001) O-Glycosylation of G-protein-coupled receptor, octopus rhodopsin. Direct analysis by FAB mass spectrometry. *FEBS Lett* 496, 19–24 [PubMed: 11343699]
68. Hurley JB (2017) Warburg's vision. *Elife* 6
69. Chinchore Y, Begaj T, Wu D, Drokhyansky E, and Cepko CL (2017) Glycolytic reliance promotes anabolism in photoreceptors. *Elife* 6
70. Das A, and Imanishi Y (2022) Drug Discovery Strategies for Inherited Retinal Degenerations. *Biology (Basel)* 11

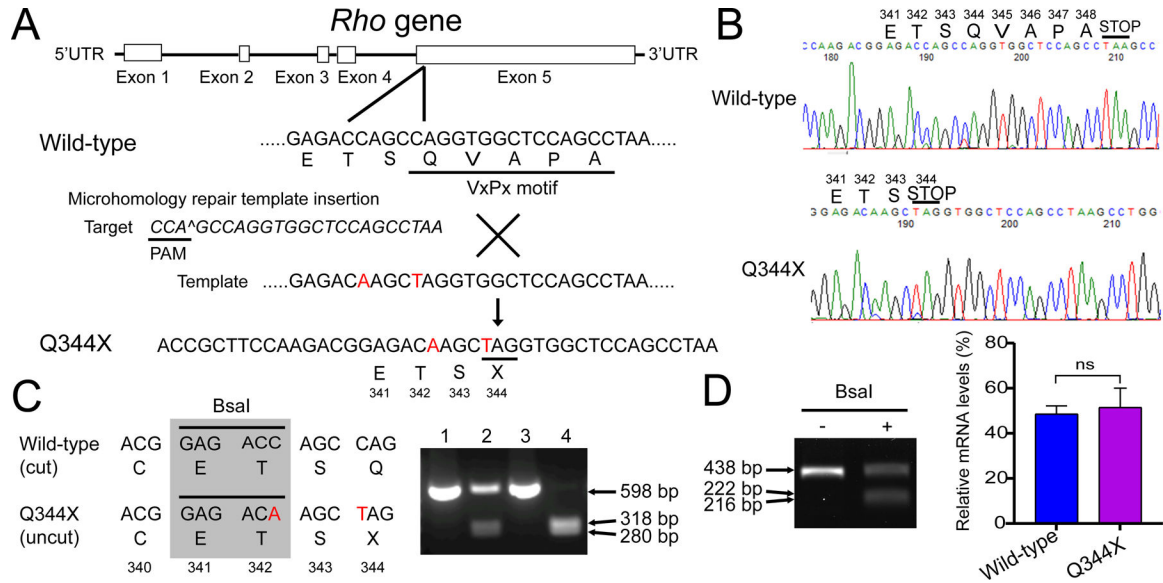


Figure 1. CRISPR/Cas9-mediated knock-in of Q344X mutation in mouse rhodopsin (*Rho*).

(A) Schematic representation of mouse *Rho* gene in chromosome 6. The PAM sequences tailored to exon 5 and microhomology template insertion site are indicated along with wild-type and Q344X alleles. The C to T conversion at the 344-position, resulting in the Q344X mutation present in exon 5 of the *Rho* gene, is highlighted in red. Another silent point mutation C to A in the codon for threonine (T) at the 342 position (highlighted in red) is introduced to prevent the recognition by guide RNA after microhomology template insertion.

(B) Validation of CRISPR/Cas9-mediated knock-in of Q344X mutation to the mouse rhodopsin gene (*Rho*) by sequencing. Upper panel shows wild-type allele with the QVAPA motif. Lower panel shows the Q344X allele with C to G mutation, leading to an early insertion of a stop codon at the 344th position.

(C) Partial sequences of exon 5 from the wild-type and Q344X rhodopsin alleles surrounding the BsaI restriction site (GAGACC) highlighted by the shaded rectangle. In the *Rho*^{Q344X} allele, the introduced silent point mutation in the codon for threonine (T) at position 342 resulted in the loss of the BsaI restriction site. Lane 1, undigested PCR fragment from a *Rho*^{Q344X/+} knock-in mouse; lane 2, same PCR fragment as lane 1 digested with BsaI; lane 3, undigested PCR fragment from a wild-type mouse; lane 4, same PCR fragment as lane 3 digested with BsaI. Upon a digestion with BsaI, a 598 bp PCR product of wild-type allele (lane 2, upper and lower fragments, respectively) was digested into two fragments (lane 4, 318 bp and 280 bp).

(D) Ratio of wild-type and Q344X mutant rhodopsin mRNA expression in the *Rho*^{Q344X/+} knock-in retina. PCR product from *Rho*^{Q344X/+} retinal cDNA was either undigested or digested with BsaI (left panel, - and +, respectively). Using real-time quantitative PCR, relative amounts of wild-type and Q344X mutant mRNA were compared (n = 3 animals). There is no significant difference in the mRNA expression levels between wild-type and Q344X mutant alleles (48.6 ± 3.6 % for wild-type and 51.5 ± 8.6 % for *Rho*^{Q344X} mRNA). ns: not significant (p = 0.6164)

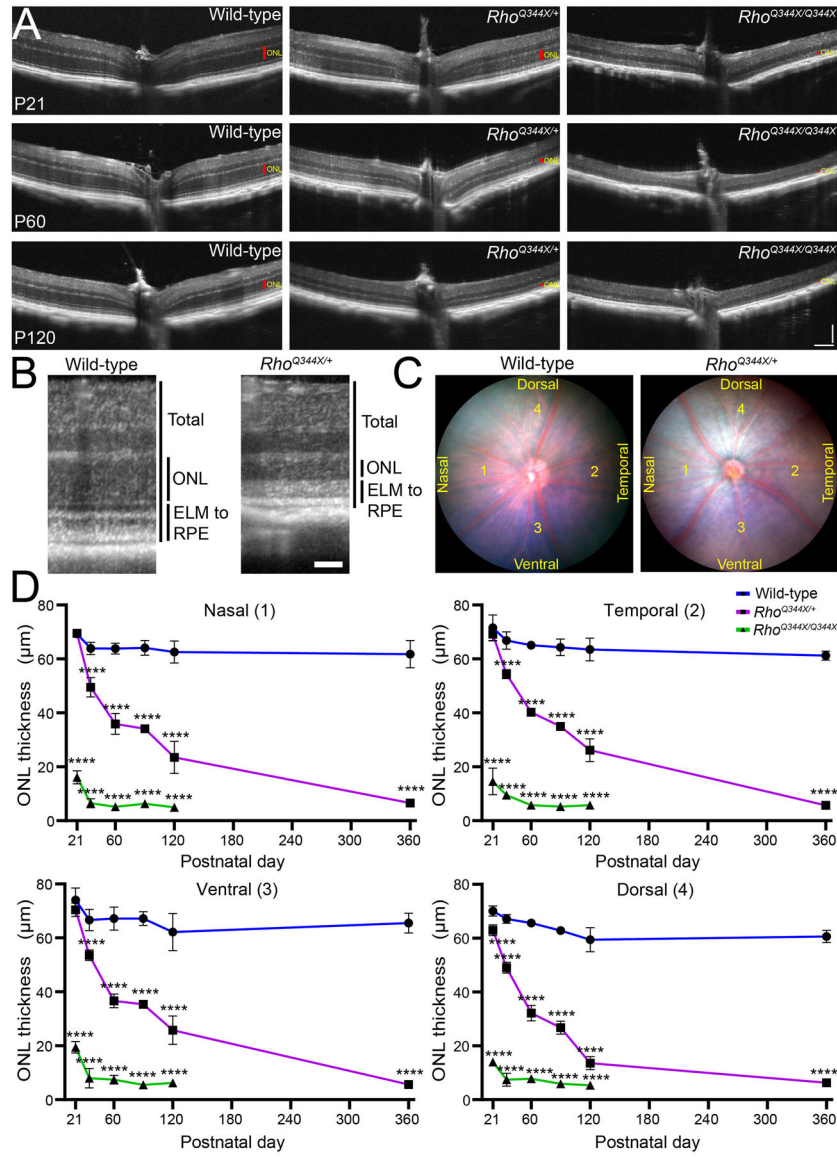


Figure 2. OCT analyses of class I *Rho*^{Q344X} knock-in mutant mouse indicate degeneration of photoreceptor neurons.

(A) OCT images for the ventral and dorsal regions including the optic nerve head (ONH) were acquired for wild-type, *Rho*^{Q344X/+}, and *Rho*^{Q344X/Q344X} mice at P21, P60, and P120. ONLs are indicated by red vertical bars. Scale bars, 100 μ m.

(B) OCT images from P60 wild-type and *Rho*^{Q344X/+} mice at the locations 500 μ m away from the ONH are shown. ELM, external limiting membrane; RPE, retinal pigment epithelium. Scale bar, 50 μ m.

(C). The thicknesses of the ONL were measured at four distinct locations situated 500 μ m away from the ONH, as illustrated in the fundus images of wild-type and *Rho*^{Q344X/+} mice.

(D) ONL thicknesses were compared among wild-type (blue), *Rho*^{Q344X/+} (magenta), and *Rho*^{Q344X/Q344X} (green) mice in four distinct regions (nasal, temporal, ventral, and dorsal) as indicated in (C). The thicknesses of the ONL were plotted as a function of postnatal days (P21 – 360), and the data were presented as mean \pm SD (n = 4 animals for each genotype).

The data were subjected to statistical analysis using two-way ANOVA, followed by Tukey's post-hoc test for pairwise comparisons. Significant differences (****, $p < 0.0001$) were observed when comparing wild-type mice to *Rho*^{Q344X/+} or *Rho*^{Q344X/Q344X} mice.

Author Manuscript

Author Manuscript

Author Manuscript

Author Manuscript

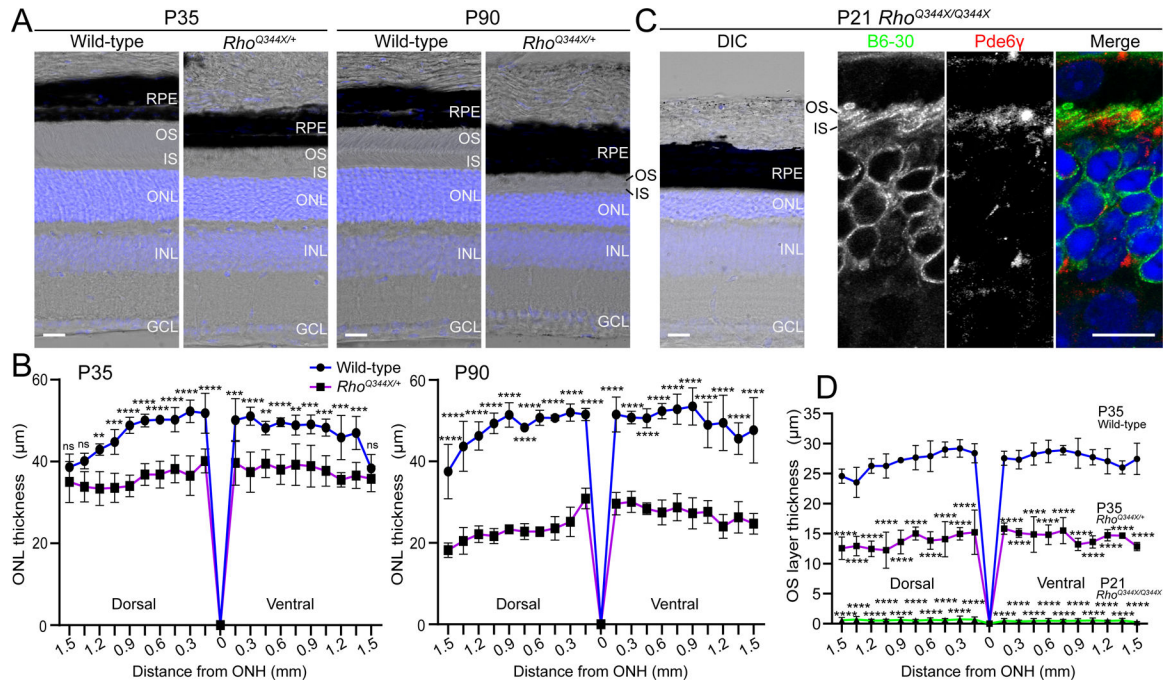


Figure 3. Histological analysis of photoreceptor cell loss in P35 and 90 *Rho*^{Q344X/+} mice.

(A) Retinal sections from wild-type and *Rho*^{Q344X/+} mice, aged P35 and P90, were labeled with Hoechst 33342 (blue) to visualize their nuclear layers. RPE: retinal pigmented epithelium, OS: outer segments, IS: inner segments, ONL: outer nuclear layer, INL: inner nuclear layer, GCL: ganglion cell layer. Scale bar, 20 µm.

(B) Thicknesses in the ONL were measured every 150 µm on the dorsal and ventral sides of the ONHs. The data show a progressive reduction of ONL thickness in *Rho*^{Q344X/+} mice due to the loss of photoreceptor cells from P35 to P90. Data were shown as mean ± SD for P35 and P90 (n = 4). The data were analyzed using two-way ANOVA. For pair-wise comparison of wild-type and *Rho*^{Q344X/+} mice, the Šídák method was utilized to calculate p-values comparing wild-type to *Rho*^{Q344X/+} mice. Statistical significance (****, $p < 0.0001$; ***, $p < 0.001$; **, $p < 0.01$) is indicated above each data point. ns: not significant ($p > 0.01$).

(C) Retinal sections from P21 *Rho*^{Q344X/Q344X} mice were labeled with Hoechst 33342 (blue) to visualize their nuclear layers (left panel). Retinal sections from P21 *Rho*^{Q344X/Q344X} mice were subjected to immunofluorescence labeling using antibodies against rhodopsin (B6–30, green) and a photoreceptor OS marker, Pde6γ (red), to label OS (right panels). DIC, differential interference contrast.

(D) Thicknesses of the OS layers from P35 wild-type mice, P35 *Rho*^{Q344X/+} mice, and P21 *Rho*^{Q344X/Q344X} mice were measured every 150 µm on the dorsal and ventral sides of the ONH. Data were presented as mean ± SD (n = 4 mice) for all the genotypes. The data were analyzed using two-way ANOVA. For pairwise comparisons, Dunnett's multiple comparison test was utilized to calculate p-values (wild-type vs. *Rho*^{Q344X/+} or wild-type vs. *Rho*^{Q344X/Q344X}, ****, $p < 0.0001$), as indicated above each data point.

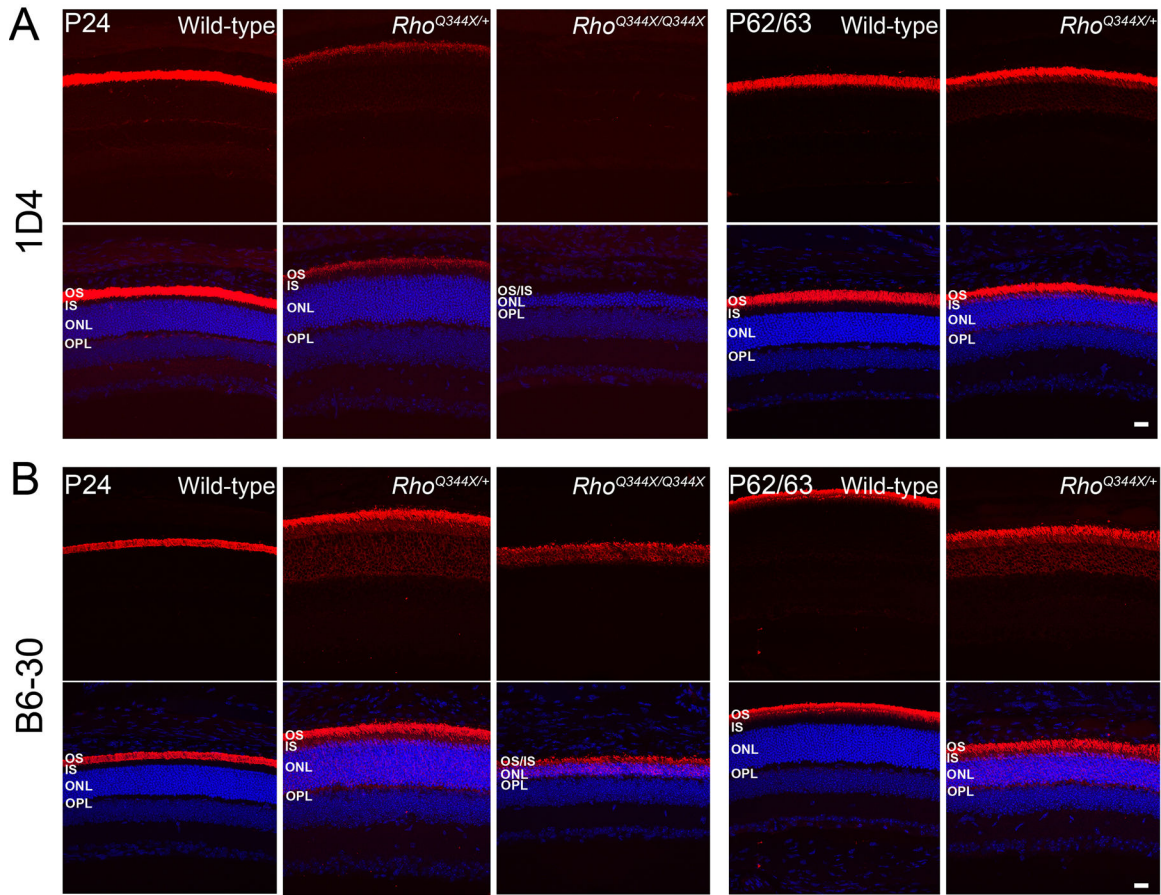


Figure 4. Rhodopsin mislocalization in *Rho*^{Q344X} knock-in mice.

(A) Retinal sections from wild-type, and *Rho*^{Q344X/+}, and *Rho*^{Q344X/Q344X} were subjected to immunofluorescent labeling using the 1D4 antibody (red). As the 1D4 recognizes the Ct epitope only present in wild-type rhodopsin protein, signals were only observed in wild-type and *Rho*^{Q344X/+} mice. Mice were studied at P24 and P62 or 63. Rhodopsin is observed mainly in the OS of wild-type mice, whereas it is also mildly mislocalized to IS, ONL and OPL in *Rho*^{Q344X/+} mice both at P24 and P62/63. OPL: outer plexiform layer

(B) Retinal sections from wild-type, *Rho*^{Q344X/+}, and *Rho*^{Q344X/Q344X} were subjected to immunofluorescent labeling using B6–30 antibody (red). As B6–30 recognizes the Nt epitope preserved both in wild-type and *RHO*^{Q344X} mutant rhodopsin, signals were observed in wild-type, *Rho*^{Q344X/+}, and *Rho*^{Q344X/Q344X} mice. Both at P24 and P62/63, signals are observed mainly in the OS of wild-type mice, whereas they are also observed in IS, ONL, and OPL of *Rho*^{Q344X/+} mice. *RHO*^{Q344X} mutant rhodopsin is significantly mislocalized to IS, ONL, OPL of *Rho*^{Q344X/Q344X} mice. Nuclei were labeled with Hoechst 33342 (blue). Scale bars, 20 μ m.

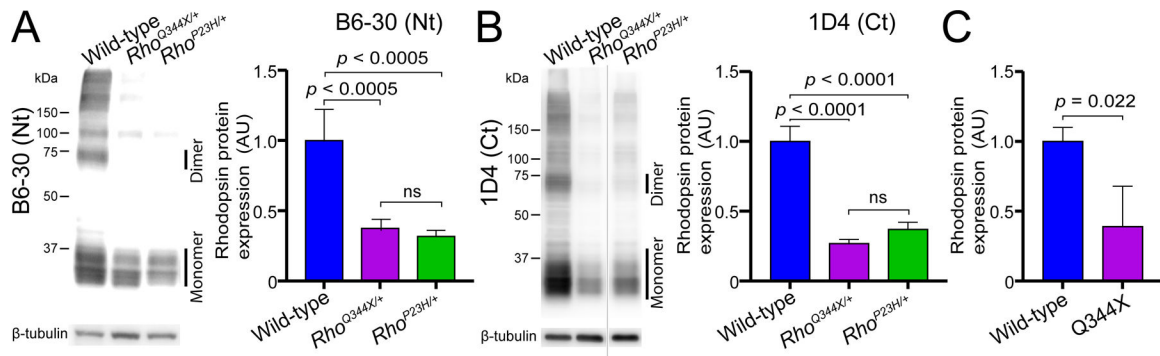


Figure 5. Rhodopsin expression is remarkably downregulated in the *Rho*^{Q344X/+} retina at P35.

Quantitative immunoblotting analysis was conducted using anti-rhodopsin monoclonal antibodies, B6–30 (Nt-specific) and 1D4 (Ct-specific) ($n = 4$ mice per genotype). Anti- β -tubulin was employed for loading controls. For quantification of signals originating from rhodopsin, we selected the regions corresponding to monomeric and dimeric forms of rhodopsin.

(A) B6–30 recognizes wild-type, RHO^{Q344X}, and RHO^{P23H} mutant rhodopsin on retinal homogenates from wild-type, *Rho*^{Q344X/+}, and *Rho*^{P23H/+} mice. Based on the analysis, total rhodopsin in the retina is significantly decreased in *Rho*^{Q344X/+}, and *Rho*^{P23H/+} retinas.

(B) The 1D4 antibody recognizes wild-type and RHO^{P23H} but is incapable of binding to RHO^{Q344X}, which lacks the Ct 5 amino acids. Based on the analysis, wild-type and RHO^{P23H} are significantly decreased in *Rho*^{Q344X/+}, and *Rho*^{P23H/+} retinas.

(C) The quantities of RHO^{Q344X} in *Rho*^{Q344X/+} retinas were calculated and compared to those of wild-type rhodopsin based on the difference in immunoblot signal intensities generated by B6–30 and 1D4 antibodies.

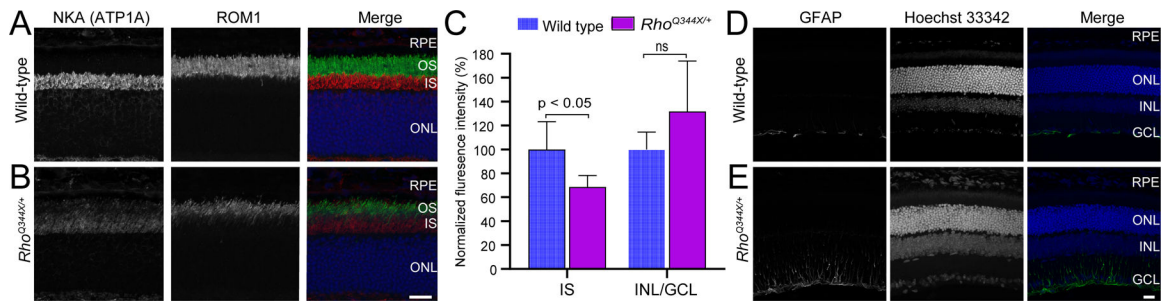


Figure 6. NKA expression is downregulated and GFAP expression is upregulated in the P35 *Rho*^{Q344X/+} retinas.

(A and B) Retinal sections from wild-type (A) and *Rho*^{Q344X/+} (B) mice were subjected to immunofluorescence labeling using antibodies against NKA (red) and ROM1 (green), a photoreceptor OS marker. Nuclei were labeled with Hoechst 33342 (blue). NKA is localized to the ISs and other regions of photoreceptors but is not observed in the OSs.

(C) Immunofluorescence originating from NKA was quantitated in IS, INL and GCL spanning 227 μm of retina length. Average intensities measured for *Rho*^{Q344X/+} were normalized to those for wild-type and the data expressed as mean \pm SD (n = 4 animals for each genotype). The data were subjected to statistical analysis using unpaired t-test for comparisons. Significant differences (*, $p < 0.05$) were observed when comparing fluorescence intensity from inner segment of wild-type mice to *Rho*^{Q344X/+} mice; ns: not significant ($p > 0.05$).

(D and E) Retinal sections from wild-type (D) and *Rho*^{Q344X/+} (E) mice were subjected to immunofluorescence labeling using antibodies against GFAP (green), a marker for astrocytes and Müller cell-mediated reactive gliosis. Nuclei were labeled with Hoechst 33342 (blue). Müller cell-mediated gliosis was activated in the P35 *Rho*^{Q344X/+} retina. Scale bars, 20 μm .

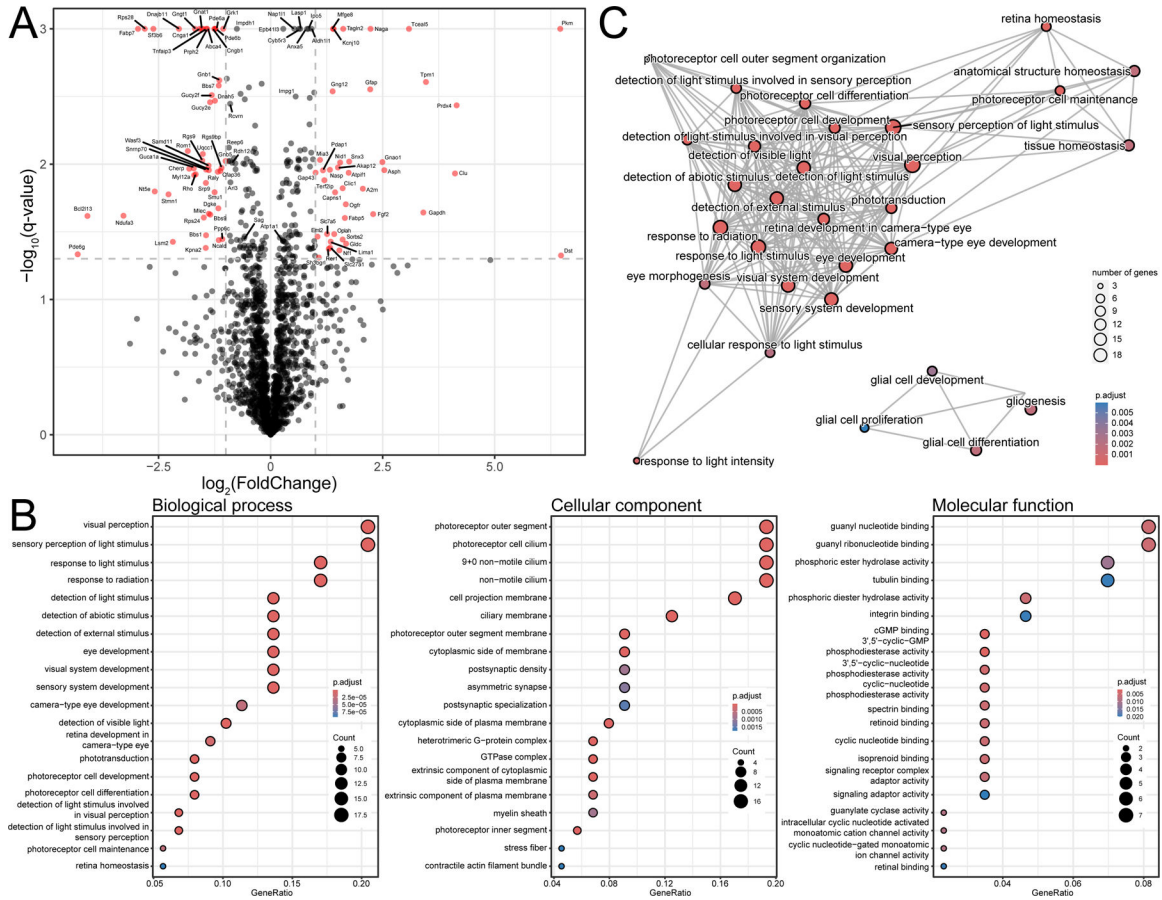


Figure 7. Differentially expressed proteins show rod outer segment proteins are downregulated in the *Rho*^{Q344X/+} retina at P35.

(A) A volcano plot for the identified proteins. X-axis shows \log_2 -transformed fold change (differential protein expression between wild-type and *Rho*^{Q344X/+} retinas), and y-axis shows $-\log_{10}$ -transformed q-value. For instance, the \log_2 -transformed fold change for Pdap1 is 1.2. This equates to a linear scale fold change of 2.4. A total of 89 proteins (shown in red) were differentially expressed with 2-fold change (\log_2 -transformed change of < -1 or > 1) and q-value < 0.05 thresholds indicated by the vertical and horizontal dashed lines.

(B) Pathway analysis for GO terms using the protein abundance with 60% threshold (a total of 93 proteins). Top 20 significantly changed pathways are shown in dot plots from top to bottom for biological process (left, adjusted $p < 0.0001$), cellular component (middle, adjusted $p < 0.005$), and molecular function (right, adjusted $p < 0.05$). The size of each dot within the plots (Count) represents the level of protein enrichment, while the color coding indicates statistical significance (p.adjust). These markers are explained within each plot.

(C) Networks illustrating the outcomes of the hypergeometric test and pathway analysis based on gene enrichment are presented. The size of each dot (Count) represents the level of gene enrichment (number of genes), while the color coding indicates statistical significance (p.adjust), as indicated in the bottom right corner of the panel.

Table 1.

Changes in retinal protein expression levels in *RhoQ344X/+* compared with wild-type at P35.

Gene symbol	Common name	Entrez ID	<i>RhoQ344X/+</i> mean protein quantity (% of wild-type)	$\log_2(\text{FoldChange})$ <i>RhoQ344X/+</i> /wild-type	$\log_2(\text{wild-type mean})$	$\log_2(\text{RhoQ344X/+ mean})$	$-\log_{10}(\text{p-value})$	q-value
<i>Rho</i>	Rhodopsin	212541	31.4	-1.67	33.89	32.22	2.918	0.012
<i>Gnat1</i>	Rod transducin alpha subunit	14685	34.4	-1.54	33.94	32.40	4.195	0.000
<i>Gnb1</i>	G-beta1 subunit	14688	44.8	-1.16	33.34	32.18	3.977	0.003
<i>Gngt1</i>	Gamma transducin 1	14699	31.1	-1.69	32.25	30.57	5.788	0.000
<i>Grk1</i>	Rhodopsin kinase	24013	48.0	-1.06	29.85	28.79	6.541	0.000
<i>Pde6a</i>	Phosphodiesterase 6A alpha subunit	225600	42.4	-1.24	29.24	28.01	6.073	0.000
<i>Pde6b</i>	Phosphodiesterase 6B beta subunit	18587	42.7	-1.23	30.61	29.38	4.355	0.000
<i>Rgs9</i>	Regulator of G protein signaling 9	19739	34.8	-1.52	27.75	26.23	2.803	0.011
<i>Gucy2e</i>	Retinal guanylyl cyclase 1 (RETGC-1)	14919	39.2	-1.35	29.91	28.55	3.831	0.016
<i>Gucy2f</i>	Retinal guanylyl cyclase 2 (RETGC-2)	245650	40.2	-1.31	25.27	23.95	3.611	0.003
<i>Cnga1</i>	cGMP-gated channel alpha subunit	12788	33.3	-1.59	28.15	26.56	4.349	0.000
<i>Cngb1</i>	cGMP-gated channel beta subunit	333329	41.9	-1.26	26.63	25.37	4.931	0.000
<i>Pprh2</i>	Peripherin	19133	37.0	-1.43	31.22	29.78	4.138	0.000
<i>Rom1</i>	Retinal outer segment membrane protein 1	19881	27.8	-1.85	31.18	29.34	3.381	0.008
<i>Abca4</i>	ATP-binding cassette transporter 4	11304	37.5	-1.42	27.75	26.34	4.936	0.000
<i>Bbs1</i>	Bardet-Biedl syndrome 1	52028	36.8	-1.44	26.40	24.96	2.025	0.034
<i>Bbs7</i>	Bardet-Biedl syndrome 7	71492	45.2	-1.14	26.21	25.06	3.867	0.002
<i>Bbs9</i>	Bardet-Biedl syndrome 9	319845	39.3	-1.35	26.63	25.28	2.158	0.024
<i>Gnat2</i>	Cone transducin alpha subunit	14686	93.4	-0.10	27.93	27.83	0.145	0.816
<i>Dnah5</i>	Dynein axonemal heavy chain 5	110082	42.3	-1.24	25.55	24.30	3.806	0.003
<i>Gltp</i>	Glial fibrillary acidic protein	14580	466.5	2.22	27.92	30.14	4.034	0.003
<i>Clu</i>	Clusterin	12759	1730.7	4.11	24.90	29.01	2.911	0.012
<i>Fgf2</i>	Fibroblast growth factor 2	14173	488.0	2.29	23.83	26.12	2.167	0.023
<i>Naga</i>	Alpha-N-acetylgalactosaminidase	17939	468.6	2.23	23.90	26.12	4.125	0.000
<i>Pkn</i>	Pyruvate kinase M	18746	8816.5	6.46	23.71	30.17	5.854	0.000
<i>Pdx4</i>	Peroxisome oxidin 4	53381	1775.3	4.15	24.54	28.69	3.843	0.004